



**HAL**  
open science

## **Tetranuclear Cr–Ln ferrocenecarboxylate complexes with a defect-dicubane structure: synthesis, magnetism, and thermolysis**

Pavel S Koroteev, Zhanna V Dobrokhotova, Andrey B Ilyukhin, Ekaterina V Belova, Alexey D Yapryntsev, Mathieu Rouzières, Rodolphe Clérac, Nikolay N Efimov

### ► To cite this version:

Pavel S Koroteev, Zhanna V Dobrokhotova, Andrey B Ilyukhin, Ekaterina V Belova, Alexey D Yapryntsev, et al.. Tetranuclear Cr–Ln ferrocenecarboxylate complexes with a defect-dicubane structure: synthesis, magnetism, and thermolysis. *Dalton Transactions*, 2021, 50, pp.16990 - 16999. 10.1039/d1dt02562g. hal-03460616

**HAL Id: hal-03460616**





**<https://hal.science/hal-03460616v1>**

Submitted on 1 Dec 2021

**HAL** is a multi-disciplinary open access archive for the deposit and dissemination of scientific research documents, whether they are published or not. The documents may come from teaching and research institutions in France or abroad, or from public or private research centers.

L'archive ouverte pluridisciplinaire **HAL**, est destinée au dépôt et à la diffusion de documents scientifiques de niveau recherche, publiés ou non, émanant des établissements d'enseignement et de recherche français ou étrangers, des laboratoires publics ou privés.

# Tetranuclear Cr–Ln ferrocenecarboxylate complexes with a defect-dicubane structure: synthesis, magnetism, and thermolysis†

Pavel S. Koroteev, \*<sup>a</sup> Zhanna V. Dobrokhotova, †<sup>a</sup> Andrey B. Ilyukhin,<sup>a</sup>  
Ekaterina V. Belova,<sup>a,b</sup> Alexey D. Yapryntsev,<sup>a</sup> Mathieu Rouzières,<sup>c</sup>  
Rodolphe Clérac \*<sup>c</sup> and Nikolay N. Efimov <sup>a</sup>

Using ferrocenecarboxylic acid (FcCO<sub>2</sub>H) and triethanolamine (H<sub>3</sub>tea) as ligands, the isostructural hetero-trimetallic complexes [Ln<sup>III</sup>Cr<sub>2</sub><sup>III</sup>(OH)<sub>2</sub>(FcCO<sub>2</sub>)<sub>4</sub>(NO<sub>3</sub>)<sub>2</sub>(Htea)<sub>2</sub>]·2MePh·2THF (Ln = Tb (**1**), Dy (**2**), Ho (**3**), Er (**4**), and Y (**5**); Fc = (η<sup>5</sup>-C<sub>5</sub>H<sub>4</sub>)(η<sup>5</sup>-C<sub>5</sub>H<sub>5</sub>)Fe; H<sub>3</sub>tea = N(CH<sub>2</sub>CH<sub>2</sub>OH)<sub>3</sub>) were obtained. In all of the complexes which possess a defective dicubane structure, two doubly deprotonated triethanolamine ligands chelate the chromium ions. However, during the synthesis of **1**, an isomeric complex **1a** in which Tb<sup>3+</sup> is chelated by triethanolamine as a tetradentate ligand, was also isolated as a few single crystals. Magnetic susceptibility measurements revealed dominant antiferromagnetic interactions in the {Ln<sup>III</sup>Cr<sub>2</sub><sup>III</sup>} cores of **1–4** leading to the formation of complexes with an uncompensated magnetic moment, while weak Cr–Cr ferromagnetic interactions were detected in the Y analogue. Complexes **1**, **2**, and **3** exhibit single-molecule magnet properties dominated by an Orbach-type relaxation mechanism with magnetization reversal barriers (Δ/k<sub>B</sub>) estimated around 54, 75, and 47 K, respectively. The Dy complex exhibits a magnetization hysteresis in an applied magnetic field at temperatures below 4 K. Thermolysis of the complexes was studied by TGA and DSC techniques; the final products obtained under an air atmosphere contain mixed oxide Cr<sub>0.75</sub>Fe<sub>1.25</sub>O<sub>3</sub> and heterotrimetallic oxide LnCr<sub>1-x</sub>Fe<sub>x</sub>O<sub>3</sub> (with x ≈ 0.75) phases.

Preparation and investigation of polynuclear 3d–4f-heterometallic complexes are an intensively developing field of modern coordination chemistry.<sup>1</sup> Due to the presence of various metal ions in close proximity, these compounds possess a wide variety of properties (magnetic, optical, catalytic, *etc.*), which makes possible their use as a basis of molecule-based functional materials.<sup>2</sup> In addition, they can serve as single-source precursors for heterometallic oxides endowed with valuable physical properties.<sup>3</sup> The combination of lanthanide ions having high magnetic anisotropy and moments, and transition metal ions capable of forming strong exchange interactions in one metallic core allows one to modulate the magnetic properties of the resulting heterometallic complexes.<sup>4</sup> The design of molecular materials based on 3d–4f-complexes that display slow relaxation of magnetization, *i.e.*, single-molecule magnet (SMM) properties, is of considerable interest.<sup>5</sup> SMMs are individual molecules, which are able to function as nanoscale magnets due to the intrinsic energy barrier of spin reversal. They represent a promising type of magnetic unit for nanotechnologies, in particular, for high-density information storage, and for molecule-based spintronic and quantum computing devices. Heterometallic 3d–4f complexes could play a particularly important role in this research field as they possess favourable characteristics to serve as SMMs, in particular, considering that lanthanide ions can potentially provide a large ground state magnetic moment and magnetic anisotropy.

In most of the heterometallic 3d–3d' and 3d–4f complexes, the bridging of various metals ions is ensured by polydentate organic ligands like Schiff base anions, aminoalcohols, amino-

<sup>a</sup>N.S. Kurnakov Institute of General and Inorganic Chemistry, Russian Academy of Sciences, GSP-1, Leninsky prosp. 31, 119991 Moscow, Russian Federation.

E-mail: pskoroteev@list.ru

<sup>b</sup>Lomonosov Moscow State University, Department of Chemistry, GSP-1, Leninskie Gory 1/3, 119991 Moscow, Russian Federation

<sup>c</sup>Univ. Bordeaux, CNRS, Centre de Recherche Paul Pascal, UMR 5031, 33600 Pessac, France. E-mail: clerac@crpp-bordeaux.cnrs.fr

phenols, amino acids, carboxylic acids and other similar ones.<sup>6</sup> However, functionalized organometallic ligands containing carboxylates and diketonate functions and a transition metal atom can also be used as chelating or bridging ligands.<sup>7</sup> The most studied functionalized organometallic ligands are ferrocene derivatives.<sup>7a,c,d</sup> In recent years, our group has obtained and studied a variety of novel complexes based on rare earth metal ions and organometallic carboxylic acids like cymantrenecarboxylic acid  $(\text{CO})_3\text{Mn}(\eta^5\text{-C}_5\text{H}_4\text{CO}_2\text{H})$ <sup>7e,f</sup> or benchrotrenecarboxylic acid  $(\text{CO})_3\text{Cr}(\eta^6\text{-C}_6\text{H}_5\text{CO}_2\text{H})$ .<sup>7g</sup> The introduction of cymantrene and ferrocene fragments into carboxylate and  $\beta$ -diketonate complexes allows one to combine the specific properties of the organometallic fragment with those of the Ln ion. In particular, the electronic properties of the ferrocene fragment can affect the magnetism of the complexes,<sup>7c</sup> while the presence of cymantrenyl fragments and lanthanide ions in the binuclear carboxylate structure can provide interesting catalytic properties.<sup>7f</sup> In addition, the obtained organometallic carboxylates and  $\beta$ -diketonates can serve as precursors for valuable heterometallic oxides with a well-controlled composition.<sup>7a,c,e-g</sup>

Complexes containing at least three different metals represent a very small family of molecular systems compared to their heterobimetallic analogues. Almost all d-d'-4f complexes described in the literature contain the second d metal ion in the form of a polycyanide anion.<sup>8</sup> As far as we know from the literature, only one carboxylate complex was reported to contain 3d (Mn) and 4f (Nd) elements linked by an additional 3d metal ion (Fe) involved in a functionalized organometallic ligand, namely, a 1,1'-ferrocenedicarboxylate ligand.<sup>9</sup> Related to this example, heterotrimetallic complexes of nickel and lanthanides  $[\text{LNi}(\text{H}_2\text{O})(\mu\text{-OAc})\text{Ln}(\text{NO}_3)_2]\cdot\text{CH}_3\text{CN}$  incorporating a polydentate Schiff base ligand, L, formed from 1,1'-diacetylferrocene dihydrazone and *o*-vanillin, are known.<sup>10</sup> In the latter case, the functionalized organometallic ligand provides coordination sites for  $\text{Ni}^{2+}$  and  $\text{Ln}^{3+}$  ions to form heterotrimetallic complexes. Therefore, it was of interest to obtain and study new complexes combining the traditional polydentate and functionalized organometallic ligands in the presence of both 3d and 4f metal ions. One of the most common types of traditional ligands used to assemble 3d-4f complexes is aminopolyols,<sup>11</sup> which often lead to tetranuclear complexes with an incomplete double cubane (defective dicubane) structure.<sup>12</sup> The present article reports the synthesis and characterization of new defect-dicubane 3d-3d'-4f-trimetallic complexes based on ferrocenecarboxylic acid and triethanolamine as core-forming ligands.

### Synthesis and structure of 1-5

Complexes  $[\text{Ln}_2\text{Cr}_2(\text{OH})_2(\text{FcCO}_2)_4(\text{NO}_3)_2(\text{Htea})_2]\cdot 2\text{MePh}\cdot 2\text{THF}$  (Ln = Tb (1), Dy (2), Ho (3), Er (4), and Y (5)) were isolated as a result of a stoichiometric reaction of  $\text{Cr}(\text{NO}_3)_3\cdot 9\text{H}_2\text{O}$  and the corresponding  $\text{Ln}(\text{NO}_3)_3\cdot n\text{H}_2\text{O}$  salts with ferrocenecarboxylic

acid (2 eq.) and triethanolamine (1 eq.) in the presence of triethylamine (5 eq.) in an alcohol/THF solvent mixture under argon. After evaporation of the solvents, the crude solid was solubilized in a 6 : 3 : 5 mixture of THF, EtOH, and toluene for crystallization by slow evaporation at room temperature. Dark-red crystals of 1, 2, 3, 4, and 5 were obtained after a few days, typically about 10 days. It is worth mentioning that these crystals are soluble in polar coordinating solvents (DMSO and DMF). In one of the syntheses involving the Tb(III) salt, several crystals of the isomeric complex 1a,  $[\text{Tb}_2\text{Cr}_2(\text{OH})_2(\text{FcCO}_2)_4(\text{NO}_3)_2(\text{Htea})_2]\cdot 2\text{MePh}\cdot 2\text{THF}$ , different from the coordinating mode of the Htea ligand, appeared on the third day. Unfortunately, it was not possible to find the appropriate conditions to obtain this complex in a reproducible manner, and thus, only its crystal structure is reported here.

As the structures of the compounds 1, 2, 3, 4, and 5 are isomorphous, only the structure of 1 will be discussed in the following; the structural information for all the studied complexes can be found in the ESI, Table S1.† The central fragment of the centrosymmetric complex  $[\text{Tb}_2\text{Cr}_2(\text{OH})_2(\text{FcCO}_2)_4(\text{NO}_3)_2(\text{Htea})_2]$  (Fig. 1a) is formed by two defective cubes  $\text{Tb}(1)\text{O}(11)\text{Tb}(1\text{A})\text{O}(11\text{A})\text{O}(5\text{A})\text{Cr}(1\text{A})\text{O}(6\text{A})$  and  $\text{Tb}(1\text{A})\text{O}(11\text{A})\text{Tb}(1)\text{O}(11)\text{O}(5)\text{Cr}(1)\text{O}(6)$ , each of which lacks one vertex and shares a common  $\text{Tb}(1)\text{O}(11)\text{Tb}(1\text{A})\text{O}(11\text{A})$  face. The Tb site has a coordination number (CN) of 8 and a coordination sphere with a strongly distorted trigonal dodecahedral geometry (trapezohedra O (2, 3, 11, 11A) and O (5, 6, 8, 9)). The O(5)N(1)O(6) atoms of the Htea ligand are coordinated to the Cr atom, while its hydroxyl arm is uncoordinated. Two crystallographically independent organometallic  $\text{FcCO}_2$  ligands additionally bridge the Tb(1) and Cr(1) centers by their carboxylate groups in a *syn-syn* coordination mode. One chelating  $\text{NO}_3^-$  anion completes the coordination sphere of the Tb(1) site. Two  $\mu_3\text{-O}$  hydroxy groups play the central role to assemble two Tb metal ions and one Cr metal ion. In the metal core of 1, the metal-metal distances are as following:  $d(\text{Tb}(1)\cdots\text{Tb}(1\text{A})) = 4.019 \text{ \AA}$ ;  $d(\text{Cr}(1)\cdots\text{Cr}(1\text{A})) = 5.244 \text{ \AA}$ ;  $d(\text{Tb}(1)\cdots\text{Cr}(1)) = 3.294 \text{ \AA}$ ;  $d(\text{Tb}(1)\cdots\text{Cr}(1\text{A})) = 3.312 \text{ \AA}$ , while the shortest intermolecular  $\text{Tb}(1)\cdots\text{Tb}(1)$ ,  $\text{Cr}(1)\cdots\text{Cr}(1)$ , and  $\text{Tb}(1)\cdots\text{Cr}(1)$  distances are 11.012, 10.506, and 9.413  $\text{ \AA}$ , respectively. It should be noted that the Htea and two of four  $\text{FcCO}_2$  ligands as well as MePh and THF lattice molecules are disordered over two positions in a 0.56 : 0.44 ratio (Fig. 1a).

In the centrosymmetric complex 1a (Fig. 1b), which has a chemical formula identical to 1, two defective cubes also have a common face. However, the Htea ligands in this complex are coordinating the Tb ions (Fig. 1b) in contrast to what is observed in the case of 1 (Fig. 1a). While two deprotonated O(5,6) Htea atoms bridge the Tb and Cr centers, the third O(7) donor atom of the protonated Htea arm is also coordinating the Tb site. Overall, the terbium CN is thus 9 with a coordination polyhedron that is closest to the three-capped trigonal prismatic geometry with O(2,6,7) and O(4,5,10) bases capped by the O(8,9) and N(1) atoms. The complex and the lattice THF molecules are ordered, while the MePh molecules are significantly disordered in a 0.61 : 0.39 ratio.

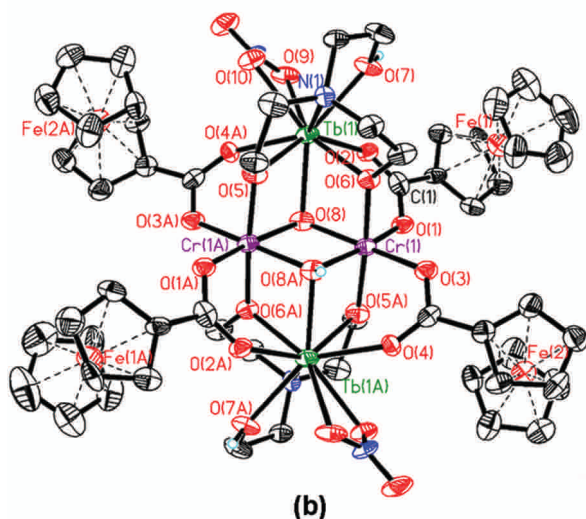
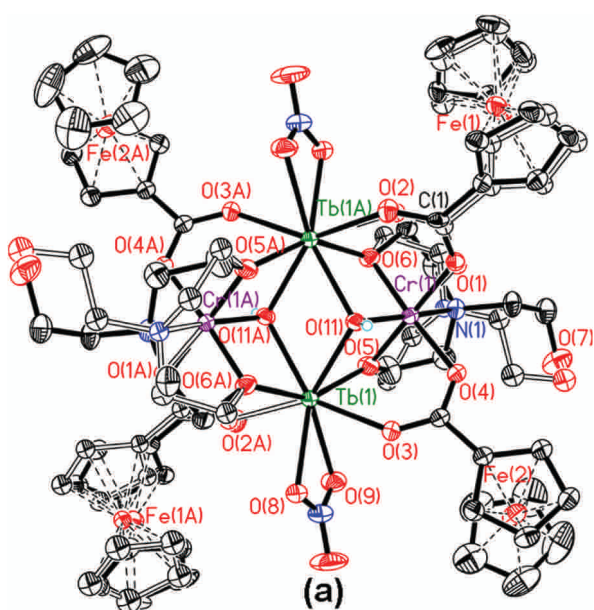


**Fig. 1** The molecular structures of the **1** (a) and **1a** (b) complexes. The H atoms at the C atoms are omitted. Two positions of disordered Fe(1, 1A) ferrocene fragments and Htea ligands in the structure of **1** are shown. Thermal ellipsoids are shown at 50% probability.

Defective dicubane structures are often found in both homo- and heterometallic tetranuclear complexes.<sup>12</sup> In the mixed-ligand complexes with a defect-dicubane  $\{Ln_2M_2O_6\}$  fragment (M is a 3d metal ion), an isomerism is possible due to the coordination of different ligands to the Ln or M metal ions (Fig. 2).  $H_3tea$  is a common ligand used in coordination chemistry to stabilize various complexes as illustrated by the presence of more than 800 compounds in CCDC (version 5.42, November 2020<sup>13</sup>). Among them, 30 compounds possess a defective dicubane fragment with Htea. In 15 compounds

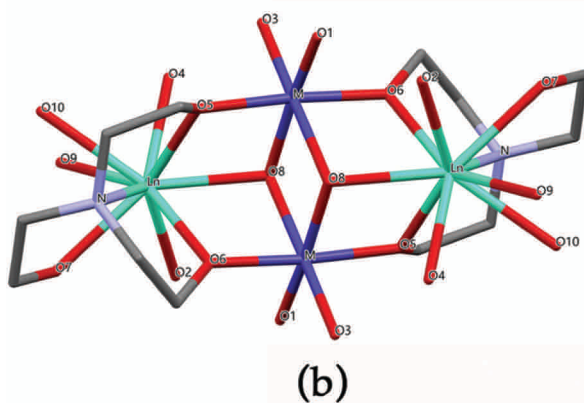
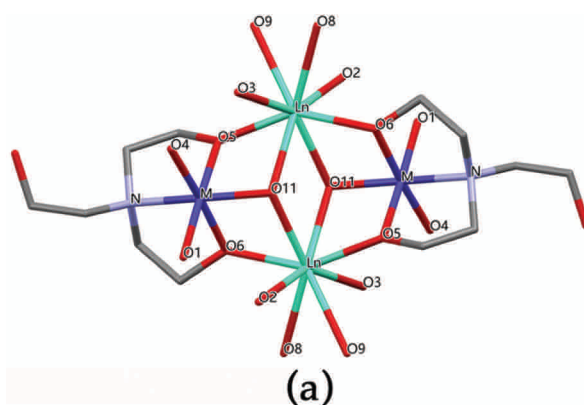


**Fig. 2** The structure of the central fragment for two types of Htea coordinations in the defect-dicubane fragment  $\{Ln_2M_2O_6\}$ .

(belonging to 6 structural types), Htea is coordinated to the 3d metal ion and in 15 other compounds (belonging to 9 structural types), to the Ln centers. In all of these compounds, the CN of the 3d metal ion is 6, and the complexes are centrosymmetric with bridging  $\mu_3$ -O(8/11) atoms belonging to hydroxy or methoxy groups. In compounds with M-N(Htea) bonds (Fig. 2a), the CN of the Ln ion is always 8 and the  $CH_2CH_2OH$  arm of the Htea ligand is not coordinated. In the case of carboxylate ligands, the O(1,2) and O(3,4) atoms belong to bridging benzoate<sup>14,15</sup> or pivalate<sup>16,17</sup> moieties. There are also three complexes based on bridging acetylacetonate ligands.<sup>18,19</sup>

In all of the compounds in which the Htea ligand is coordinated to the Ln ions, the carboxylate ligands are present, therefore, the resulting molecular structures are very similar, with a Ln CN of 9. The deprotonated O(5,6) atoms of the Htea ligand adopt a chelate-bridging mode while the hydroxyl O(7) atom takes part in chelating the Ln ion (Fig. 2b). In two published compounds, the O(1,3) and O(2,4) atoms belong to carboxylates, and the O(9,10) atoms belong to the chelating  $NO_3$  group.<sup>20</sup> A similar structure was found in compound **1a**. In the other 13 compounds, all the remaining O(1,3), O(2,4) and O(9,10) coordinating atoms are provided by chelating carboxylate ligands.<sup>21–24</sup>

### Thermolysis of the complexes

It has been shown earlier that the thermolysis of carboxylate and  $\beta$ -diketonate 3d–4f complexes containing transition metal in an organometallic (ferrocene,<sup>7a,c</sup> cymantrene,<sup>7ef</sup> or benchrotrone<sup>7g</sup>) moiety brings about 3d–4f-mixed oxides, which are valuable functional materials. In the case of cymantrenecarboxylates, the stoichiometry of the resulting oxide is determined exclusively by using the metals' ratio in the starting complex.<sup>7ef</sup> Therefore, the study and analysis of the thermal decomposition of 3d–3d'–4f-trimetallic complexes are of great interest and potentially can lead to the discovery of new functional oxides.

Thermolysis of complexes 1–5 was studied in atmospheres of argon and air. In both cases, the thermal decomposition of the complexes occurs stepwise, and the main characteristics of the process are independent of the nature of the rare-earth metal ion. Therefore, the results for the Ho complex 3 are taken as an illustrating example for the whole series of compounds (Fig. 3, 4, and S1†). The first step of the decomposition both in air and in an inert atmosphere in the temperature range of 110–160 °C results in a weight loss of  $14.5 \pm 1.5\%$  and

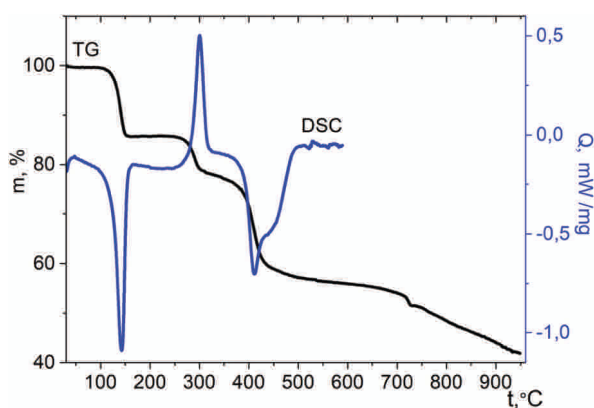


Fig. 3 Thermolysis of complex 3 under argon.

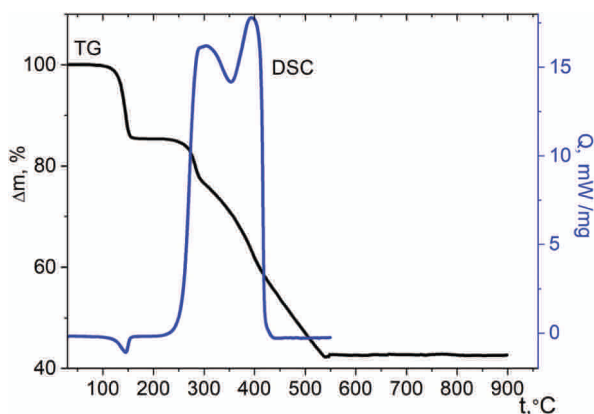


Fig. 4 Thermolysis of complex 3 under air.

is accompanied by an endotherm. This stage obviously corresponds to the simultaneous removal of lattice THF and toluene (their content calculated from the molecular formula is 15.4%). Selected ion currents in the mass spectrum during this stage confirm the loss of THF ( $m/z = 72$  [ $C_4H_8O$ ,  $M$ ]<sup>+</sup>, 71 [ $C_4H_7O$ ]<sup>+</sup>, 44 [ $C_2H_4O$ ]<sup>+</sup>) and toluene:  $m/z = 91$  [ $C_7H_7$ ]<sup>+</sup>, 92 [ $C_7H_8$ ,  $M$ ]<sup>+</sup>, 65 [ $C_5H_5$ ]<sup>+</sup> (ref. 25) (Fig. S1†). The desolvated compound is then stable under argon up to 270 °C. At higher temperature, under an argon atmosphere, the second step (270–320 °C) begins; it is exothermic and is accompanied by a weight loss of  $8.5 \pm 1.5\%$ . This stage, most probably, corresponds to the intramolecular process of oxidation of the organic parts of the molecule by  $NO_3$  groups. The calculated content of  $NO_3$  groups is 5.82%; the weight loss during this stage is greater due to the elimination of the oxidized organic part. The mass spectrum of the gas phase in this temperature region contains ion current peaks with  $m/z = 30$  [ $NO$ ]<sup>+</sup>, 44 [ $CO_2$ ]<sup>+</sup>, and 17 [ $HO$ ]<sup>+</sup> (the latter corresponds to water molecules). Similar exothermic processes in the 261–290 °C temperature range were previously observed for the thermolysis of the  $[Nd(H_2tea)](NO_3)_2$  complex, which also contained deprotonated  $H_3tea$  and  $NO_3$  groups.<sup>26</sup> Between 320 and 370 °C, the mass loss remains small. Above 370 °C, a complex-shaped endothermic peak is detected with a third mass loss of  $21.3 \pm 1.5\%$  between 370 and 520 °C. This stage corresponds to the complete decomposition of organic parts of the complex with a partial elimination of the ferrocene, which is gaseous in this temperature range (b.p. = 249 °C). The mass spectrum of the gas phase in this temperature range contains the peaks corresponding to ferrocene ( $m/z = 186$  [ $C_{10}H_{10}Fe$ ,  $M$ ]<sup>+</sup>, 121 [ $C_5H_5Fe$ ]<sup>+</sup>, 56 [ $Fe$ ]) and the peaks that may be attributed to the volatile products of dehydration of  $H_3tea$ , trivinylamine ( $m/z = 95$  [ $C_6H_9N$ ,  $M$ ]<sup>+</sup>), and divinylethanolamine ( $m/z = 82$  [ $C_5H_8N$ ,  $M - CH_2OH$ ]<sup>+</sup>; Fig. S1†). Earlier we have also observed the evolution of ferrocene during thermolyses of ferrocenecarboxylate<sup>7a</sup> and ferrocenylacetone<sup>7c</sup> rare earth complexes under argon. At higher temperatures, the mass loss decreases and does not reach completion even at 950 °C. The final product of the thermolysis under argon is amorphous.

When thermolysis under air is studied, a fast weight loss above 260 °C accompanied by a strong exothermic effect is observed (Fig. 4). This stage corresponds obviously to the oxidation of the organic parts of the desolvated molecule. This process ends at around 540 °C and leads to the mass loss of  $43.5 \pm 1.5\%$ . The weight of the solid residue,  $42.5 \pm 1.5\%$  of the initial sample, is close to the calculated content for  $M_2O_3$  oxides ( $M = Ho, Cr, Fe$ ) expected as the product of the oxidative thermolysis (40%).

In order to obtain a better crystallinity of the final products, the thermolysis under air was followed by annealing at 950 °C during an hour. According to the powder X-ray diffraction analyses, the annealed products contain the perovskite  $LnMO_3$  ( $M = Cr$  or  $Fe$ ) and mixed oxide  $Cr_{0.75}Fe_{1.25}O_3$  phases (Fig. S2†). As the  $LnCrO_3$  and  $LnFeO_3$  phases are isomorphous and continuous solid solutions  $LnCr_{1-x}Fe_xO_3$  can be formed,<sup>27</sup> it is virtually impossible to distinguish them by powder X-ray diffrac-

**Table 1** Mean ratio of metals in the products of thermolysis of 1–5 under air determined by EDXMA

Complex	Mean ratio of metals, atomic percent		
	Ln	Cr	Fe
1 (Tb)	22.63	21.47	55.90
2 (Dy)	24.27	24.75	50.98
3 (Ho)	25.18	24.86	49.95
4 (Er)	25.09	24.70	50.21
5 (Y)	24.40	25.95	49.65

tion analysis. Therefore, energy dispersive X-ray microanalyses (EDXMA) of the thermolysis products were carried out and revealed a metal Ln:Cr:Fe ratio close to 1:1:2 (Table 1, Tables S2a–e, Fig. S3a–e†). Thus, a rough chemical formula of the thermolysis product is  $\text{LnCrFe}_2\text{O}_6$ , which corresponds well to the initial metal ratio of the complexes. Remarkably, this ratio seems to persist during thermolysis under air despite the volatility of the ferrocene. Since the second phase present in the thermolysis product is  $\text{Cr}_{0.75}\text{Fe}_{1.25}\text{O}_3$ , the estimated formula for the trimetallic perovskite phase is  $\text{LnCr}_{0.25}\text{Fe}_{0.75}\text{O}_3$ . These types of oxide phases can represent interesting magnetic materials<sup>27a,c</sup> or possess multiferroic properties like those studied in the  $\text{YCr}_{1-x}\text{Fe}_x\text{O}_3$  oxide systems.<sup>27c,d</sup>

### Magnetic properties

The magnetic properties of the polynuclear 3d–4f complexes are generally interesting to explore considering the large magnetic moment inherent to most of the Ln ions and the possibility of magnetic exchange with, and between, 3d-metal ion spins.<sup>2d,4,5</sup> For the complexes containing highly anisotropic lanthanide ions (like 1–4), SMM properties are often observed.<sup>2d</sup> In the present complexes, the  $\text{Ln}^{3+}$  and  $\text{Cr}^{3+}$  metal ions are fully responsible for the observed paramagnetic properties as the ferrocene fragments contain  $\text{Fe}^{\text{II}}$  in its low-spin diamagnetic  $d^6$  configuration.<sup>7a–c,28</sup>

The  $\chi T$  values experimentally determined at 300 K for complexes 1–5 are given in Table 2. They are close to the theoretical values for two  $\text{Ln}^{3+}$  (ref. 4) and two  $\text{Cr}^{3+}$  ( $S = 3/2$ ,  $g = 2$ ,  $C_{\text{theor}} = 1.875 \text{ cm}^3 \text{ K mol}^{-1}$ )<sup>29</sup> magnetically isolated centers. The thermal dependences of the magnetic susceptibility for complexes 1–3 are somewhat similar, as shown by the  $\chi T$  vs.  $T$  plots in Fig. 5. In the 300–100 K range, the  $\chi T$  product decreases only slightly, while below 100 K, the decrease of the  $\chi T$  value is more pronounced until it reaches a plateau around 25–16 K for 1, and minima at 42 and 28 K for 2 and 3, respectively.

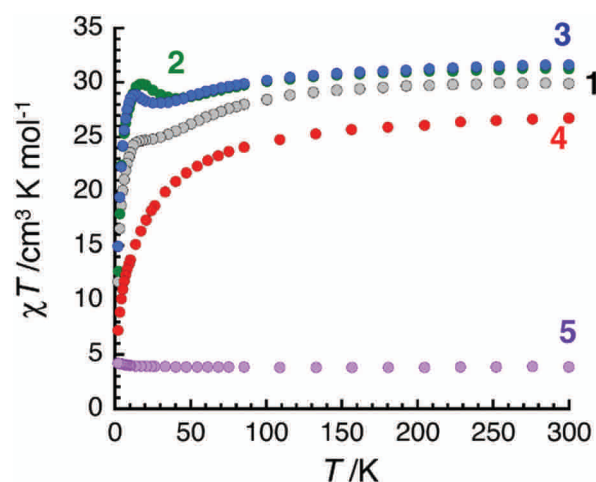


**Fig. 5** Temperature dependences of the  $\chi T$  products (where  $\chi$  is the molar magnetic susceptibility) collected in an applied dc magnetic field of 0.5 T for complexes 1–5.

ively. At lower temperature, the  $\chi T$  product for 1 further decreases to  $11.7 \text{ cm}^3 \text{ K mol}^{-1}$  at 2 K. In contrast, the  $\chi T$  products for the Dy and Ho analogues (2 and 3) show maxima at 18 and 14 K before decreasing down to 12.7 and  $15.0 \text{ cm}^3 \text{ K mol}^{-1}$  at 2 K. These complex thermal behaviours underline the presence of an exchange coupling scheme (probably involving antiferromagnetic interactions<sup>30</sup>) in these three compounds leading to uncompensated magnetic moments in the  $\{\text{Ln}_2^{\text{III}}\text{Cr}_2^{\text{III}}\}$  cores. Furthermore, the final decrease of the  $\chi T$  product below 10 K is likely due to the intrinsic magnetic anisotropy of the lanthanide ions and/or possible inter-complex antiferromagnetic interactions. In the case of the Er complex 4, the  $\chi T$  value is continuously decreasing over the entire temperature range with significant acceleration below 100 K suggesting the predominance of antiferromagnetic interactions in the metallic  $\{\text{Er}_2^{\text{III}}\text{Cr}_2^{\text{III}}\}$  core. A similar thermal variation of the magnetic susceptibility was reported earlier for the analogous series of benzoate complexes,  $[\text{Ln}_2\text{Cr}_2(\text{OMe})_2(\text{O}_2\text{CPh})_4(\text{mdea})_2(\text{NO}_3)_2]$ , with a defective dicubane structure containing twice deprotonated *N*-methyl-diethanolamine ( $\text{H}_2\text{mdea}$ ) as a backbone ligand.<sup>30a,31</sup>

For complex 5 containing diamagnetic yttrium centers, the  $\chi T$  value remains constant down to 20 K, after which a slight increase down to 2 K is observed. This magnetic behaviour indicates that very weak ferromagnetic interactions are present between the  $\text{Cr}^{3+}$  spins in the  $\{\text{Y}_2^{\text{III}}\text{Cr}_2^{\text{III}}\}$  core and, by extrapolation, in the  $\{\text{Ln}_2^{\text{III}}\text{Cr}_2^{\text{III}}\}$  core of the whole series of complexes.

**Table 2** Magnetic characteristics obtained from the dc susceptibility data of 1–5

	1 (Tb)	2 (Dy)	3 (Ho)	4 (Er)	5 (Y)
$\chi T$ (at 300 K), $\text{cm}^3 \text{ K mol}^{-1}$	29.9	31.3	31.6	26.7	3.88
$C_{\text{theor}}$ , $\text{cm}^3 \text{ K mol}^{-1}$	27.38	32.09	31.88	26.70	3.75
$\chi T$ (at $T$ ), $\text{cm}^3 \text{ K mol}^{-1}(\text{K})$	24.7 (18 K)	29.9 (18 K)	28.9 (14 K)	—	—
$\chi T$ (at 2 K), $\text{cm}^3 \text{ K mol}^{-1}$	11.7	12.7	15.0	7.3	4.2

A simple Heisenberg  $S = 3/2$  spin dimer model (with  $\mathbf{H} = -2J\mathbf{S}_1\mathbf{S}_2$ ) can be used to estimate these magnetic interactions at about +90 mK. Due to the geometry of the  $\{\text{Ln}^{\text{III}}\text{Cr}_2^{\text{III}}\}$  core (Fig. 2a), this ferromagnetic interaction is simply reinforcing the most probable  $\text{Ln}^{\text{III}}\cdots\text{Cr}^{\text{III}}$  antiferromagnetic interactions which leads to an uncompensated spin topology.

For complex 2, the field dependence of the magnetization below 4 K exhibits a significant hysteresis effect revealing the presence of the slow dynamics of the magnetization (Fig. 6). The coercive field estimated at 2 K is relatively large (1.6 T). The magnetization at 2 K, which increases almost linearly between 1 and 7 T, does not show a clear saturation even at the highest accessible magnetic field, where it reaches  $9.8 \mu_{\text{B}}$ . The step features observed at 2 K are likely related to fast relaxation processes like quantum tunneling of the magnetization (QTM) close to zero field and resonant QTM around 2.5 T. These fast relaxation pathways seem to disappear when the temperature is increased as the step features are almost completely absent at 3 K. It cannot be completely excluded that the weak antiferromagnetic  $\text{Dy}^{\text{III}}\cdots\text{Cr}^{\text{III}}$  interactions also play a role in these anomalies. Earlier, a pronounced magnetic hysteresis was found for defect-dicubane complexes, in which  $\text{Dy}^{\text{III}}\cdots\text{Cr}^{\text{III}}$  antiferromagnetic interactions were also observed.<sup>30a,b</sup>

The slow dynamics of the magnetization, *i.e.* single-molecule magnet properties, have been observed in numerous mono/polynuclear homo/heterometallic lanthanide-based complexes, in particular, in those containing highly anisotropic lanthanide ions like Dy,<sup>32</sup> Tb,<sup>33</sup> Ho,<sup>34</sup> or Er.<sup>35</sup> Therefore, ac susceptibility measurements have been performed for complexes 1–5 to probe the magnetization dynamics observed in Fig. 6 for 2 and, eventually, to extract the characteristic temperature dependence of the relaxation time. As shown in Fig. S4, S5, and S6† for 1, 2, and 3, respectively, an out-of-phase ac-signal ( $\chi''$ ) is observed, typically below 15 K in zero dc-field, which contrasts with the Er and Y complexes that maintain a zero  $\chi''$  signal down to 2 K (between 10 and 10 000 Hz). The characteristic relaxation time and its associated esti-

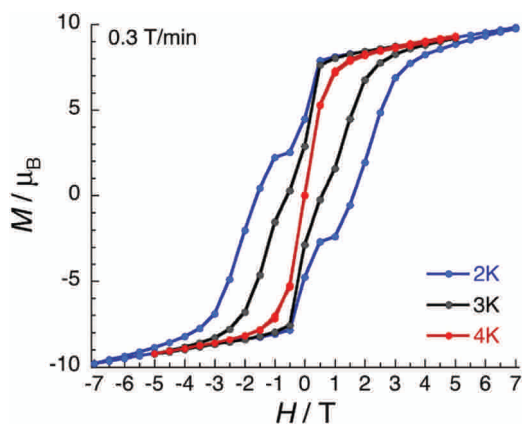


Fig. 6 Field dependence of the magnetization,  $M$ , for Dy complex 2, below 4 K (scanning at  $0.3 \text{ T min}^{-1}$ ).

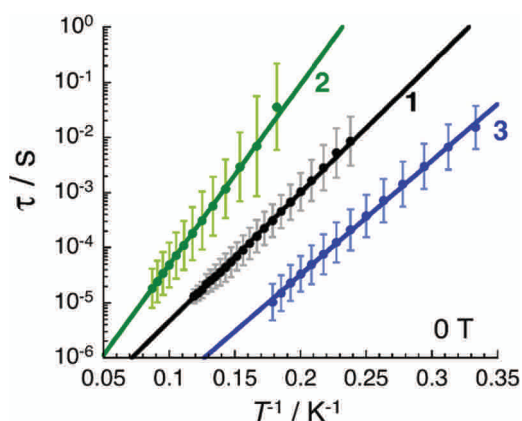


Fig. 7 Temperature dependences of the relaxation time for 1–3 estimated from the generalised Debye fits of the ac susceptibility data shown in Fig. S4–S6† collected under zero applied field. The estimated standard deviations of the relaxation time (vertical solid bars) have been calculated from the  $\alpha$  parameters of the generalised Debye fit and the log-normal distribution as described in ref. 38. The solid lines represent the best fit discussed in the text.

mated standard deviation (ESD) were evaluated for these three complexes as a function of the temperature (Fig. 7) from the fitting of the experimental ac susceptibility data shown in Fig. S4–S6† to the generalised Debye model.<sup>36–38</sup>

When a dc magnetic field is applied during the ac measurements (Fig. S7–S9†), the characteristic frequency of the relaxation mode is not strongly modified suggesting the absence of a modification of the relaxation pathway under an applied magnetic field at 5.5, 7, and 4 K for complexes 1, 2 and 3, respectively. In contrast, for the Er analogue 4, a relaxation mode clearly appears around 6000 Hz under a field of about 0.1 T (Fig. S10†). Unfortunately, due to the proximity of this relaxation mode to the end of our ac frequency experimental window, it was not possible to follow its temperature dependence. In the case of complex 5, no out-of-phase ac signal was detected at 2 K even in an applied magnetic field.

In the absence of a dc-field, the dynamics of the paramagnetic relaxation<sup>37–39</sup> is well-known to be dominated by the three independent mechanisms including the Raman,<sup>39,40</sup> Orbach-like (thermally activated)<sup>39,41</sup> and QTM<sup>39</sup> relaxation pathways, as summarised in the following equations:

$$\tau^{-1} = \tau_{\text{Raman}}^{-1} + \tau_{\text{Orbach}}^{-1} + \tau_{\text{QTM}}^{-1} \quad (1)$$

$$\tau^{-1} = CT^n + \tau_0^{-1} \exp\left(-\frac{\Delta}{k_{\text{B}}T}\right) + \tau_{\text{QTM}}^{-1} \quad (2)$$

when the relaxation times are plotted as  $\tau$  vs.  $T^{-1}$ , as shown in Fig. 7, clear straight lines are observed as expected for an Orbach-like relaxation process (see eqn (2)).<sup>40,41</sup> Hence, the dominant relaxation mechanism in the 4.2–8.4 K, 5.5–11.5 K, and 3–5.6 K ranges for 1, 2, and 3, respectively, is the Orbach-like one with  $\Delta/k_{\text{B}}$  equal to 54(3), 75(5), and 47(2) K and the relaxation attempt time,  $\tau_0$ , equal to 21, 26, and  $2 \times 10^{-9}$  s, respectively. No deviation from this thermally activated regime,

which could be the signature of the QTM (likely observed for complex 2 below 3 K in Fig. 6) or Raman (non-exponential variation) processes, is observed.

The SMM properties of analogous benzoate complexes possessing the same central metallic core,  $[\text{Cr}_2\text{Ln}_2(\text{OMe})_2(\text{O}_2\text{CPh})_4(\text{mdea})_2(\text{NO}_3)_2]$ , have earlier been reported.<sup>30a,31</sup> The experimental  $\Delta/k_B$  values were found to be 64 K for the Tb complex,<sup>31</sup> 77 K for the Dy derivative,<sup>30a</sup> and 52 K for the Ho-based analogue.<sup>31</sup> Remarkably, the energy gap follows the same trend as that in the present family of compounds with the Dy derivative exhibiting the highest value. For the Er complex, the energy barrier could not be determined;<sup>31</sup> the same is observed for complex 4. In the benzoate series of complexes, the introduction of electron acceptor substituents to the benzoate ligand (namely, the substitution of phenyl by 2-chloro-4,5-difluorophenyl, improving the acceptor properties of the carboxylate ligand) improved significantly the SMM properties of the compounds ( $\Delta/k_B = 89$  K for  $\{\text{Cr}_2\text{Dy}_2\}$  complex), which contrasts with the decrease of the SMM energy gap of a dysprosium analogue (to 65 K) when a donor *tert*-butyl substituent was attached to the *para*-position of the phenyl group.<sup>42</sup> The strength of the acceptor or donor properties of a given substituent at the carboxylic group can be evaluated from the acid strength. Therefore, to evaluate the effect of a substituent on the electron density, it is convenient to compare the  $\text{p}K_a$  value of the corresponding acids.<sup>43</sup> For example, benzoic acid has a  $\text{p}K_a$  value of 4.20 (water, 25 °C) which is lower than that of the 4-*tert*-butylbenzoic acid one, 4.36 (under the same conditions), as expected due to the effect of a functional group with more electron-donating substituents in the second case.<sup>44</sup> For ferrocenecarboxylic acid, the  $\text{p}K_a$  value is 7.66 in dioxane-water medium (70% dioxane), which is higher than 7.32 determined for the benzoic acid under the same conditions.<sup>43</sup> The replacement of the phenyl group with ferrocenyl shifts the  $\text{p}K_a$  value of the acid towards weaker acidity, similarly to the replacement of phenyl with 4-*tert*-butylphenyl. This simple analysis suggests a stronger electron donor effect of the ferrocenyl substituent in the ferrocenecarboxylate ligand compared to that of phenyl in the benzoate ligand, and thus, one should expect a noticeable decrease of the SMM energy gap from 77 K for  $\{\text{Cr}_2\text{Dy}_2\}$  complex 2. However, the decrease of the SMM energy gap for 2 (75 K) is minimal and remains within the error bar of the measurements. The SMM properties of 1–4 compare indeed very well with those of the benzoate analogues. Thus, the most important factor for the SMM properties of these defective dicubane  $\{\text{Cr}_2\text{Ln}_2\}$  complexes is not the nature of the carboxylate ligand, but definitely the structure and the composition of the metal core.

In summary, we obtained a new family of 3d–3d'–4f-heterotrimetallic complexes containing an organometallic ferrocenecarboxylate fragment,  $[\text{Ln}_2^{\text{III}}\text{Cr}_2^{\text{III}}(\text{OH})_2(\text{FcCO}_2)_4(\text{NO}_3)_2(\text{Htea})_2] \cdot 2\text{MePh} \cdot 2\text{THF}$  (Ln = Tb, Dy, Ho, Er, and Y). These compounds

possess a defective dicubane structure often found for tetranuclear metal complexes. Thermolysis of these molecular systems in air affords mixtures of  $\text{Cr}_{0.75}\text{Fe}_{1.25}\text{O}_3$  phases and  $\text{LnCr}_{0.25}\text{Fe}_{0.75}\text{O}_3$  trimetallic perovskite-like mixed oxides. The paramagnetic properties of these complexes were also studied; they are dominated by weak antiferromagnetic interactions between the  $\text{Ln}^{\text{III}}$  and  $\text{Cr}^{\text{III}}$  magnetic centers, which leads to uncompensated magnetic moments in the  $\{\text{Ln}_2^{\text{III}}\text{Cr}_2^{\text{III}}\}$  cores. Combined dc and ac susceptibility measurements revealed the slow dynamics of the magnetization, *i.e.* the single-molecule magnet properties of the Tb, Dy, Ho and Er analogues, with the dysprosium complex displaying the largest magnetization reversal barrier around 75 K and a 1.6 T magnetic hysteresis at 2 K.

## Materials and methods

The following commercial reagents and solvents were used for the syntheses: hydrated lanthanide nitrates ( $\text{Ln}(\text{NO}_3)_3 \cdot n\text{H}_2\text{O}$ ,  $n = 6$  for Tb, Dy; or 5 for Ho, Er, and Y) and chromium nitrate ( $\text{Cr}(\text{NO}_3)_3 \cdot 9\text{H}_2\text{O}$ ) from Alfa Aesar; ferrocenecarboxylic acid  $\text{FcCO}_2\text{H}$  and triethanolamine from Aldrich; solvents ( $\text{CH}_3\text{CN}$ ,  $\text{CH}_3\text{OH}$ , THF, EtOH, and toluene) from Alfa Aesar. All experiments in solutions were carried out in foil-wrapped vessels to prevent photolysis. Acetonitrile and toluene were distilled over  $\text{P}_2\text{O}_5$  and  $\text{CaH}_2$  successively; methanol was distilled over magnesium; THF was distilled over  $\text{LiAlH}_4$ .

Elementary analyses were carried out using an EA1108 85 automatic C, H, N, S analyzer (Carlo Erba Instruments).

The attenuated total reflection infrared (ATR-IR) spectra of the complexes were recorded in the range of 400–3000  $\text{cm}^{-1}$  on a Bruker ALPHA instrument.

Scanning electron microscopy (SEM) and energy dispersive X-ray microanalysis (EDXMA) of the thermolysis products were performed using a Carl Zeiss NVision 40 microscope equipped with an Oxford Instruments X-Max EDX detector at accelerating voltages of 3–20 kV.

The magnetic susceptibility measurements were performed with the use of an MPMS-XL Quantum Design SQUID magnetometer and PPMS-9 susceptometer. These experimental systems work between 1.8 and 400 K at dc applied fields ranging from –7 to 7 T (MPMS-XL). The ac susceptibility data were measured with oscillating ac fields of 1 to 6 Oe at frequencies between 10 and 10 000 Hz (PPMS-9). Measurements were performed on analytically pure polycrystalline samples (44.5, 38.8, 34.9, 19.63 and 48.5 mg for 1, 2, 3, 4, and 5, respectively) introduced in polyethylene bags ( $3 \times 0.5 \times 0.02$  cm, typically between 7 to 25 mg) and restrained in mineral oil (typically between 7 to 33 mg). Prior to the experiments,  $M$  vs.  $H$  measurements were performed at 100 K to confirm the absence of ferromagnetic impurities. Consistent dc susceptibility and in-phase ac susceptibility have been obtained between 1.85 and 15 K. The magnetic data were corrected for the sample holder, the mineral oil and the diamagnetic contribution.



### Synthesis of [Ln<sub>2</sub>Cr<sub>2</sub>(OH)<sub>2</sub>(FcCO<sub>2</sub>)<sub>4</sub>(NO<sub>3</sub>)<sub>2</sub>(Htea)<sub>2</sub>]-2MePh-2THF (Ln = Tb (1 and 1a), Dy (2), Ho (3), Er (4), and Y (5))

In a CH<sub>3</sub>OH (6 mL) and THF (6 mL) solvent mixture, Cr(NO<sub>3</sub>)<sub>3</sub>·9H<sub>2</sub>O (400 mg, 1 mmol) and Ln(NO<sub>3</sub>)<sub>3</sub>·*n*H<sub>2</sub>O (1 mmol) were dissolved with stirring. Triethanolamine (150 mg, 1 mmol) in 1 mL of EtOH was added to the reaction mixture that was subsequently stirred for 30 minutes. With intensive stirring, FcCO<sub>2</sub>H (460 mg, 2 mmol) was then added. Triethylamine (0.70 mL, 5 mmol) was added, and the reaction mixture was stirred under argon for 24 hours. Then the mixture was evaporated to dryness *in vacuo*, and the residue was extracted with a mixture of THF (6 mL), EtOH (3 mL) and toluene (5 mL). The solution was filtered and allowed to evaporate slowly at room temperature. X-ray suitable dark-red crystals were formed during ten days. They were washed with EtOH, toluene, and hexane and air-dried. The yields were 40–45%.

In the case of Tb, in one of the syntheses, several crystals of the isomeric complex **1a** appeared on the third day. Unfortunately, it was not possible to find the right conditions to synthesize this complex reproducibly, and thus it was only characterized by single-crystal X-ray crystal diffraction.

For **1**, anal. calc. for C<sub>78</sub>H<sub>96</sub>Cr<sub>2</sub>Fe<sub>4</sub>N<sub>4</sub>O<sub>24</sub>Tb<sub>2</sub>: C, 44.21; H, 4.57; N, 2.64. Found: C, 44.40; H, 4.50; N, 2.67. IR of **1**: 3479 w, 3214 br, 3104 w, 2971 w, 2950 w, 2868 w, 1556 m, 1465 s, 1436 s, 1382 s, 1342 vs, 1294 m, 1189 m, 1105 m, 1092 m, 1069 m, 1020 m, 1000 m, 960 w, 942 w, 919 m, 903 m, 878 m, 837 m, 813 s, 802 m, 775 s, 731 s, 694 m, 657 m, 622 m, 596 m, 515 vs, 484 vs, 464 vs, 419 m.

For **2**, anal. calc. for C<sub>78</sub>H<sub>96</sub>Cr<sub>2</sub>Dy<sub>2</sub>Fe<sub>4</sub>N<sub>4</sub>O<sub>24</sub>: C, 44.07; H, 4.55; N, 2.64. Found: C, 44.21; H, 4.45; N, 2.59. IR of **2**: 3481 w, 3249 br, 3090 w, 2973 w, 2945 w, 2910 w, 2863 w, 1556 m, 1465 s, 1436 s, 1385 s, 1345 vs, 1292 m, 1192 m, 1105 m, 1092 m, 1065 m, 1024 m, 1000 m, 940 m, 920 m, 906 m, 875 m, 840 m, 814 s, 800 m, 779 s, 738 s, 698 m, 663 m, 623 m, 598 m, 573 m, 521 vs, 477 vs, 467 vs, 425 m.

For **3**, anal. calc. for C<sub>78</sub>H<sub>96</sub>Cr<sub>2</sub>Fe<sub>4</sub>Ho<sub>2</sub>N<sub>4</sub>O<sub>24</sub>: C, 43.97; H, 4.54; N, 2.63. Found: C, 43.95; H, 4.49; N, 2.57. IR of **3**: 3484 w, 3271 br, 3086 w, 2971 w, 2945 w, 2906 w, 2862 w, 1548 s, 1467 s, 1436 s, 1385 s, 1345 vs, 1294 m, 1194 m, 1093 m, 1063 m, 1024 m, 1000 m, 940 m, 920 m, 908 m, 875 m, 840 m, 814 s, 800 m, 779 s, 738 s, 698 m, 625 m, 598 m, 575 m, 521 vs, 480 vs, 467 vs, 421 m.

For **4**, anal. calc. for C<sub>78</sub>H<sub>96</sub>Cr<sub>2</sub>Fe<sub>4</sub>Er<sub>2</sub>N<sub>4</sub>O<sub>24</sub>: C, 43.87; H, 4.53; N, 2.62. Found: C, 43.95; H, 4.46; N, 2.65. IR of **4**: 3474 w, 3349 br, 3086 w, 2981 w, 2947 w, 2862 w, 1559 m, 1546 m, 1467 s, 1436 s, 1384 s, 1355 vs, 1296 m, 1191 m, 1090 s, 1068 m, 1020 m, 1000 m, 940 m, 920 m, 906 m, 875 m, 813 s, 800 m, 776 s, 738 s, 698 m, 624 m, 599 m, 575 m, 511 vs, 479 vs, 469 vs, 419 m.

For **5**, anal. calc. for C<sub>78</sub>H<sub>96</sub>Cr<sub>2</sub>Fe<sub>4</sub>Y<sub>2</sub>N<sub>4</sub>O<sub>24</sub>: C, 47.34; H, 4.89; N, 2.83. Found: C, 47.46; H, 4.81; N, 2.79. IR of **5**: 3484 w, 3271 br, 3088 w, 2971 w, 2945 w, 2909 w, 2863 w, 1546 s, 1466 s, 1436 s, 1385 s, 1345 vs, 1296 m, 1192 m, 1093 s, 1066 m, 1022 m, 1000 m, 940 m, 920 m, 908 m, 819 m, 800 m, 779 s,

736 s, 698 m, 623 m, 598 m, 575 m, 521 vs, 479 vs, 469 vs, 422 m.

### X-ray data collection

The single crystal X-ray diffraction data sets were collected on a Bruker SMART APEX II diffractometer equipped with a CCD camera and a graphite monochromated MoK $\alpha$  radiation source.<sup>45</sup> Semi-empirical absorption corrections for all complexes were applied.<sup>46</sup> The structures were solved by direct methods using Fourier techniques and were refined by the full-matrix least squares against  $F^2$  with anisotropic thermal parameters for all non-hydrogen atoms. The hydrogen atoms were positioned geometrically and refined using the riding model. All calculations were carried out with the use of the SHELX-2016/6 program package.<sup>47</sup> The crystallographic parameters and the refinement statistics are given in Table S1.†

The Powder X-ray diffraction patterns were recorded on a Bruker D8 ADVANCE X-Ray Diffractometer (CuK $\alpha$ , Ni-filter, LYNXEYE detector, reflection geometry).

### Thermal analysis

The thermal decomposition of the compounds was studied by differential scanning calorimetry (DSC) and thermogravimetry (TGA) under a flow (20 mL min<sup>-1</sup>) of artificial air (O<sub>2</sub>, (20.9 ± 0.5) vol%; N<sub>2</sub>, (79.1 ± 0.5) vol%; CH<sub>4</sub>, CO, CO<sub>2</sub>, <0.005 vol%) and argon (Ar, >99.998%; O<sub>2</sub>, 0.0002%; N<sub>2</sub>, <0.001%; aqueous vapor, <0.0003%; CH<sub>4</sub>, <0.0001%). Thermogravimetric measurements were performed on a TG 209 F1 instrument in alundum crucibles at a heating rate of 10 °C min<sup>-1</sup> in the range of 30–950 °C (under argon) or 30–900 °C (under air). The composition of the gas phase was studied using a QMS 403C Aëolos mass-spectrometric unit under TGA experiment conditions. The ionizing electron energy was 70 eV; the largest determined mass number (the mass-to-charge ratio) was 300 amu. The weight of the samples was 0.5 to 3.0 mg. Differential scanning calorimetry studies were carried out on a DSC 204 F1 instrument in aluminum cells at a heating rate of 10 °C min<sup>-1</sup> in the range of 30–590 °C (under argon) or 30–550 °C (under air). Each experiment was repeated at least three times. The thermobalance was calibrated using the phase transition points of standard compounds. The calorimeter was calibrated by temperature (based on the phase transition parameters of standard compounds: cyclohexane, Hg, Ga, benzoic acid, KNO<sub>3</sub>, In, Sn, Bi, and CsCl of 99.99% purity) and by phase transition enthalpies according to ISO 11357-1. Data of thermal analysis methods were analyzed according to ISO 11357-1, ISO 11357-2, ISO 11358, and ASTM E 1269-95 standards using the NETZSCH Proteus Thermal Analysis software package.

Conceptualization, Pavel S. Koroteev and Nikolay N. Efimov; methodology, Zhanna V. Dobrokhotova; thermal analysis, Ekaterina V. Belova; synthesis, Pavel S. Koroteev; X-ray study,

Andrey B. Ilyukhin; magnetic studies, Nikolay N. Efimov, Rodolphe Clérac and Mathieu Rouzières; EDXMA study, Alexey D. Yapyrintsev; writing – original draft preparation, Pavel S. Koroteev; writing – review and editing, Nikolay N. Efimov and Rodolphe Clérac; supervision, Nikolay N. Efimov.

This research was funded by the Ministry of Science and Higher Education of the Russian Federation, grant number 075-15-2020-779.

This research was partially performed using the equipment of the JRC PMR IGIC RAS. This work was supported by the CNRS, the University of Bordeaux, the Région Nouvelle Aquitaine and Quantum Matter Bordeaux.

- 1 (a) C. Huang, *Rare earth coordination chemistry: fundamentals and applications*, John Wiley & Sons, Singapore, 2010, pp. 91–137; (b) R. Janicki, A. Mondry and P. Starynowicz, *Coord. Chem. Rev.*, 2017, **340**, 98–133; (c) Z. Majeed, G. E. Kostakis, Y. Lana and A. K. Powell, *Dalton Trans.*, 2011, **40**, 12210–12216.
- 2 (a) E. Coronado, J. R. Galan-Mascaros and C. Marti-Gastaldo, *Inorg. Chem.*, 2007, **46**(20), 8108–8110; (b) Q.-Y. Chen, Q.-H. Luo, D.-G. Fu and J.-T. Chen, *J. Chem. Soc., Dalton Trans.*, 2002, 2873–2287; (c) J.-P. Costes, F. Dahan and A. Dupuis, *Inorg. Chem.*, 2000, **39**, 165–168; (d) R. Sessoli and A. K. Powell, *Coord. Chem. Rev.*, 2009, **253**, 2328–2341; (e) B.-H. Ye, M.-L. Tong and X.-M. Chen, *Coord. Chem. Rev.*, 2005, **249**, 545–565.
- 3 (a) O. Carp, L. Patron, A. Ianculescu, D. Crisan, N. Dragan and R. Olar, *J. Therm. Anal. Calorim.*, 2003, **72**, 253–261; (b) L. G. Hubert-Pfalzgraf, *J. Mater. Chem.*, 2004, **14**, 3113–3123; (c) H. Lu, D. S. Wright and S. D. Pike, *Chem. Commun.*, 2020, **56**, 854–871; (d) P. S. Koroteev, Zh. V. Dobrokhotova and V. M. Novotortsev, *Russ. J. Gen. Chem.*, 2018, **88**, 1306–1317.
- 4 C. Benelli and D. Gatteschi, *Chem. Rev.*, 2002, **102**, 2369–2387.
- 5 (a) Y.-G. Huang, F.-L. Jiang and M.-Ch. Hong, *Coord. Chem. Rev.*, 2009, **253**, 2814–2834; (b) B. Wang, S. Jiang, X. Wang and S. Gao, *Sci. China, Ser. B: Chem.*, 2009, **52**, 1739–1758; (c) J.-L. Liu, J.-Y. Wu, Y.-C. Chen, V. Mereacre, A. K. Powell, L. Ungur, L. F. Chibotaru, X.-M. Chen and M.-L. Tong, *Angew. Chem., Int. Ed.*, 2014, **53**(47), 12966–12970; (d) J. Wang, M. Feng, M. N. Akhtar and M.-L. Tong, *Coord. Chem. Rev.*, 2019, **387**, 129–153; (e) Y. Zhou, M. Hong and X. Wu, *Chem. Commun.*, 2006, 135–143; (f) K. Liu, W. Shi and P. Cheng, *Coord. Chem. Rev.*, 2015, **289–290**, 74–122; (g) J. Lu, M. Guo and J. Tang, *Chem. – Asian J.*, 2017, **12**(21), 2772–2779; (h) A. V. Funes and P. Alborés, *Eur. J. Inorg. Chem.*, 2018, **20–21**, 2067–2089; (i) Y. Peng, M. K. Singh, V. Mereacre, C. E. Anson, G. Rajaraman and A. K. Powell, *Chem. Sci.*, 2019, **10**, 5528–5538; (j) Z. G. Lada, E. Katsoulakou and S. P. Perlepes, *Synthesis and Chemistry of Single-molecule Magnets in Single-Molecule Magnets. Molecular Architectures and Building Blocks for Spintronics*, ed. M. Hołynska, Wiley-VCH, Weinheim, 2019, pp. 245–303; (k) B. Monteiro, J. T. Coutinho and L. C. J. Pereira, *Heterometallic 3d-4f SMMs in Lanthanide-Based Multifunctional Materials*, Elsevier, 2018, pp. 233–261.
- 6 M. Sakamoto, K. Manseki and H. Okawa, *Coord. Chem. Rev.*, 2001, **219–221**, 379–414.
- 7 (a) P. S. Koroteev, Zh. V. Dobrokhotova, N. N. Efimov, A. B. Ilyukhin and V. M. Novotortsev, *Russ. J. Coord. Chem.*, 2014, **40**(7), 495–504, and references therein; (b) N. N. Efimov, P. S. Koroteev, A. V. Gavrikov, A. B. Ilyukhin, Zh. V. Dobrokhotova and V. M. Novotortsev, *Magnetochemistry*, 2016, **2**(4), 38; (c) P. S. Koroteev, Zh. V. Dobrokhotova, A. B. Ilyukhin, N. N. Efimov, M. Rouzières, M. A. Kiskin, R. Clérac and V. M. Novotortsev, *Dalton Trans.*, 2016, **45**, 6405–6417, and references therein; (d) H. Hou and L. Li, Progress in Ferrocene Carboxylate Metal Complexes, in *Leading Edge Organometallic Chemistry Research*, Nova Science Publishers, 2006, pp. 27–74, and references therein; ; (e) P. S. Koroteev, A. B. Ilyukhin, K. A. Babeshkin, E. V. Belova, A. V. Gavrikov and N. N. Efimov, *Eur. J. Inorg. Chem.*, 2021, **2**, 147–155, and references therein; (f) P. S. Koroteev, Zh. V. Dobrokhotova, A. B. Ilyukhin, N. N. Efimov, A. V. Gavrikov and V. M. Novotortsev, *Russ. J. Coord. Chem.*, 2016, **42**, 591–603; (g) A. V. Gavrikov, P. S. Koroteev, N. N. Efimov, Zh. V. Dobrokhotova, A. B. Ilyukhin, A. K. Kostopoulos, A.-M. Ariciu and V. M. Novotortsev, *Dalton Trans.*, 2017, **46**, 3369–3380.
- 8 M. Andruh, *Chem. Commun.*, 2018, **54**, 3559–3577, and references therein.
- 9 V. Mereacre, A. M. Ako, G. Filoti, J. Bartolomé, C. E. Anson and A. K. Powell, *Polyhedron*, 2010, **29**, 244–247.
- 10 A. Chakraborty, P. Bag, E. Rivière, T. Mallah and V. Chandrasekhar, *Dalton Trans.*, 2014, **43**, 8921–8932.
- 11 J. W. Sharples and D. Collison, *Coord. Chem. Rev.*, 2014, **260**, 1–20.
- 12 (a) P. S. Koroteev, N. N. Efimov, A. B. Ilyukhin, Zh. V. Dobrokhotova and V. M. Novotortsev, *Inorg. Chim. Acta*, 2014, **418**, 157–162, and references therein; (b) S. Meghdadi, V. Mirkhani and K. Mereiter, *C. R. Chim.*, 2015, **18**(6), 654–661; (c) A. Paul, V. Bertolasi, A. Figuerola and S. C. Manna, *J. Solid State Chem.*, 2017, **249**, 29–38; (d) T. N. Nguyen, Kh. A. Abboud and G. Christou, *Polyhedron*, 2013, **66**, 171–178; (e) L. Jiang, D.-Y. Zhang, J.-J. Suo, W. Gu, J.-L. Tian, X. Liu and S.-P. Yan, *Dalton Trans.*, 2016, **45**(25), 10233–10248; (f) Z. You, K. Prsa, J. Mutschler, S. N. Herringer, J. Wang, Y. Luo, B. Zheng,

- S. Decurtins, K. W. Krämer, O. Waldmann and S.-X. Liu, *ACS Omega*, 2020, **6**(1), 483–491; (g) Y. Wang, D. Wang, W. Shu, J. Sha and H. Zhang, *Transition Met. Chem.*, 2020, **45**, 245–251; (h) H. Zhang, J. Zhang, Y. Li, Y. Qin, Y. Chen, W. Liu, D. Gao and W. Li, *J. Coord. Chem.*, 2015, **68**(16), 2798–2809.
- 13 C. R. Groom, I. J. Bruno, M. P. Lightfoot and S. C. Ward, *Acta Crystallogr., Sect. B: Struct. Sci., Cryst. Eng. Mater.*, 2016, **72**(2), 171–179.
- 14 S. K. Langley, N. F. Chilton, L. Ungur, B. Moubaraki, L. F. Chibotaru and K. S. Murray, *Inorg. Chem.*, 2012, **51**, 11873–11881.
- 15 S. K. Langley, D. P. Wielechowski, B. Moubaraki, B. F. Abrahams and K. S. Murray, *Aust. J. Chem.*, 2014, **67**, 1581–1587.
- 16 A. V. Funes, L. Carrella, E. Rentschler and P. Alborés, *Dalton Trans.*, 2014, **43**, 2361–2364.
- 17 A. V. Funes, L. Carrella, Y. Rechkemmer, J. van Slageren, E. Rentschler and P. Alborés, *Dalton Trans.*, 2017, **46**, 3400–3409.
- 18 S. K. Langley, N. F. Chilton, B. Moubaraki and K. S. Murray, *Inorg. Chem.*, 2013, **52**, 7183–7192.
- 19 S. K. Langley, N. F. Chilton, B. Moubaraki and K. S. Murray, *Inorg. Chem. Front.*, 2015, **2**, 867–875.
- 20 S. Mukherjee, M. R. Daniels, R. Bagai, K. A. Abboud, G. Christou and C. A. Lampropoulos, *Polyhedron*, 2010, **29**, 54–65.
- 21 A. Baniodeh, Y. Lan, G. Novitchi, V. Mereacre, A. Sukhanov, M. Ferbinteanu, V. Voronkova, C. E. Anson and A. K. Powell, *Dalton Trans.*, 2013, **42**, 8926–8938.
- 22 V. Mereacre, A. Baniodeh, C. E. Anson and A. K. Powell, *J. Am. Chem. Soc.*, 2011, **133**, 15335–15337.
- 23 A. Baniodeh, V. Mereacre, N. Magnani, Y. Lan, J. A. Wolny, V. Schunemann, C. E. Anson and A. K. Powell, *Chem. Commun.*, 2013, **49**, 9666–9668.
- 24 M. Murugesu, A. Mishra, W. Wernsdorfer and K. A. Abboud, *Polyhedron*, 2006, **25**, 613–625.
- 25 NIST Chemistry WebBook. Available online: <http://webbook.nist.gov>.
- 26 H. Icbudak, V. T. Yilmaz and H. Olmez, *Thermochim. Acta*, 1996, **289**, 23–32.
- 27 (a) X. Liu, L. Hao, Y. Liu, X. Ma, S. Meng, Y. Li, J. Gao, H. Guo, W. Han, K. Kai Sun, M. Wu, X. Chen, L. Xie, F. Klose and D. Chen, *J. Magn. Magn. Mater.*, 2016, **417**, 382–388; (b) W. Hu, Y. Chen, H. Yuan, G. Zhang, G. Li, G. Pang and S. Feng, *J. Solid State Chem.*, 2010, **183**, 1582–1587; (c) S. Kovachev, D. Kovacheva, S. Aleksovska, E. Svab and K. Krezhov, *J. Optoelectron. Adv. Mater.*, 2009, **11**(10), 1549–1552; (d) B. Rajeswaran, P. Mandal, R. Saha, E. Suard, A. Sundaresan and C. N. R. Rao, *Chem. Mater.*, 2012, **24**, 3591–3595.
- 28 L. N. Mulay and M. E. Fox, *J. Chem. Phys.*, 1963, **38**, 760–764.
- 29 Yu. V. Rakin and V. T. Kalinnikov, *Sovremennaya magneto-khimiya [Modern Magnetochemistry]*, Nauka, St.Petersburg, 1994, 272 pp. (in Russian).
- 30 (a) S. K. Langley, D. P. Wielechowski, V. Vieru, N. F. Chilton, B. Moubaraki, B. F. Abrahams, L. F. Chibotaru and K. S. Murray, *Angew. Chem., Int. Ed.*, 2013, **52**, 12014–12019; (b) S. K. Langley, D. P. Wielechowski, V. Vieru, N. F. Chilton, B. Moubaraki, L. F. Chibotaru and K. S. Murray, *Chem. Sci.*, 2014, **5**, 3246–3256; (c) L. Qin, J. Singleton, W.-P. Chen, H. Nojiri, L. Engelhardt, R. E. P. Winpenny and Y.-Zh. Zheng, *Angew. Chem., Int. Ed.*, 2017, **56**, 16571–16574.
- 31 S. K. Langley, D. P. Wielechowski, N. F. Chilton, B. Moubaraki and K. S. Murray, *Inorg. Chem.*, 2015, **54**(21), 10497–10503.
- 32 D. N. Woodruff, R. E. P. Winpenny and R. A. Layfield, *Chem. Rev.*, 2013, **113**(7), 5110–5148.
- 33 K. Katoh, S. Yamashita, N. Yasuda, Y. Kitagawa, B. K. Breedlove, Y. Nakazawa and M. Yamashita, *Angew. Chem., Int. Ed.*, 2018, **57**(30), 9262–9267.
- 34 T. Kajiwara, *Angew. Chem., Int. Ed.*, 2017, **56**, 11306–11308.
- 35 Sh.-D. Jiang, B.-W. Wang, H.-L. Sun, Zh.-M. Wang and S. Gao, *J. Am. Chem. Soc.*, 2011, **133**, 4730–4733.
- 36 K. S. Cole and R. H. Cole, *J. Chem. Phys.*, 1941, **9**, 341–351.
- 37 A. Abragam and B. Bleaney, *Electron Paramagnetic Resonance of Transition Ions*, Clarendon Press, Oxford, 1970.
- 38 D. Reta and N. F. Chilton, *Phys. Chem. Chem. Phys.*, 2019, **21**, 23567–23575.
- 39 K. N. Shrivastava, *Phys. Status Solidi*, 1983, **117**, 437–458.
- 40 J. H. Van Vleck, *Phys. Rev.*, 1940, **57**, 426–447.
- 41 R. Orbach, *Proc. R. Soc. London, Ser. A*, 1961, **264**, 458–484.
- 42 S. K. Langley, D. P. Wielechowski, B. Moubaraki and K. S. Murray, *Chem. Commun.*, 2016, **52**, 10976–10979.
- 43 É. G. Perevalova, K. I. Grandberg, N. A. Zharikova, S. P. Gubin and A. N. Nesmeyanov, *Russ. Chem. Bull.*, 1966, **15**, 796–802.
- 44 M. Ludwig, V. Baron, K. Kalfus, O. Pytela and M. Večeřa, *Collect. Czech. Chem. Commun.*, 1986, **51**, 2135–2142.
- 45 *SMART (Control) and SAINT (Integration) Software, Version 5.0*, Bruker AXS Inc., Madison, WI, 1997.
- 46 G. M. Sheldrick, *SADABS, Program for Scanning and Correction of Area Detector Data*, Göttingen University, Göttingen, Germany, 2003.
- 47 G. M. Sheldrick, Crystal structure refinement with SHELXL, *Acta Crystallogr., Sect. C: Struct. Chem.*, 2015, **71**(1), 3–8.

**SUPPLEMENTARY MATERIALS**

**Table S1.** Crystal data and structure refinement for **1 – 5** and **1a**.

Identification code	<b>1</b>	<b>2</b>	<b>3</b>	<b>4</b>	<b>5</b>
Empirical formula	$C_{78}H_{96}Cr_2Fe_4N_4O_{24}Tb_2$	$C_{78}H_{96}Cr_2Dy_2Fe_4N_4O_{24}$	$C_{78}H_{96}Cr_2Fe_4Ho_2N_4O_{24}$	$C_{78}H_{96}Cr_2Er_2Fe_4N_4O_{24}$	$C_{78}H_{96}Cr_2Fe_4N_4O_{24}Y_2$
Formula weight	2118.82	2125.98	2130.84	2135.50	1978.80
Temperature, K	150(2)	150(2)	150(2)	150(2)	150(2)
Wavelength, Å	0.71073	0.71073	0.71073	0.71073	0.71073
Crystal system	Monoclinic	Monoclinic	Monoclinic	Monoclinic	Monoclinic
Space group	$P2_1/n$	$P2_1/n$	$P2_1/n$	$P2_1/n$	$P2_1/n$
$a$ , Å	15.0231(4)	15.2812(4)	15.2579(5)	14.9585(4)	15.0033(5)
$b$ , Å	17.2324(5)	16.7770(5)	16.7324(5)	17.2006(5)	17.1273(5)
$c$ , Å	15.6619(4)	15.8983(5)	15.9113(5)	15.6650(5)	15.6663(5)
$\beta$ , °	99.7370(10)	103.1360(10)	103.0660(10)	99.7280(10)	100.1480(10)
Volume, Å <sup>3</sup>	3996.21(19)	3969.2(2)	3957.0(2)	3972.6(2)	3962.7(2)
$Z$	2	2	2	2	2
$D$ (calc), Mg/m <sup>3</sup>	1.761	1.779	1.788	1.785	1.658
$\mu$ , mm <sup>-1</sup>	2.789	2.909	3.029	3.138	2.500
$F(000)$	2132	2136	2140	2144	2028
Crystal size, mm	$0.3 \times 0.3 \times 0.2$	$0.4 \times 0.3 \times 0.28$	$0.24 \times 0.24 \times 0.16$	$0.2 \times 0.2 \times 0.2$	$0.32 \times 0.3 \times 0.12$
$\theta$ range, °	2.101, 29.603	2.064, 30.544	2.067, 28.715	2.106, 30.046	2.102, 29.180
Index ranges	-20 $\leq h \leq$ 20 -23 $\leq k \leq$ 23 -21 $\leq l \leq$ 21	-21 $\leq h \leq$ 21 -23 $\leq k \leq$ 23 -22 $\leq l \leq$ 22	-19 $\leq h \leq$ 20 -22 $\leq k \leq$ 22 -21 $\leq l \leq$ 21	-21 $\leq h \leq$ 20 -24 $\leq k \leq$ 23 -21 $\leq l \leq$ 22	-19 $\leq h \leq$ 20 -22 $\leq k \leq$ 22 -21 $\leq l \leq$ 20
Reflections collected	53330	55260	50647	54182	50517
Independent reflections, $R_{int}$	11218, 0.0515	12036, 0.0376	10141, 0.0469	11600, 0.0487	10360, 0.0525
Completeness to $\theta = 25.242^\circ$	99.9 %	100.0 %	100.0 %	99.9 %	99.9 %
Absorption correction	Semi-empirical from equivalents	Semi-empirical from equivalents	Semi-empirical from equivalents	Semi-empirical from equivalents	Semi-empirical from equivalents
Max., min. transmission	0.7459, 0.6117	0.7461, 0.5241	0.7458, 0.5678	0.746, 0.607	0.7458, 0.556
Refinement method	Full-matrix least-squares on $F^2$	Full-matrix least-squares on $F^2$	Full-matrix least-squares on $F^2$	Full-matrix least-squares on $F^2$	Full-matrix least-squares on $F^2$
Data / restraints / parameters	11218 / 0 / 595	12036 / 15 / 595	10141 / 15 / 594	11600 / 0 / 595	10360 / 0 / 595
Goodness-of-fit	0.974	0.999	0.974	0.923	1.068
$R_1, wR_2$ [ $I > 2\sigma(I)$ ]	0.0335, 0.0788	0.0316, 0.0814	0.0302, 0.0709	0.0309, 0.0722	0.0381, 0.0824
$R_1, wR_2$ (all data)	0.0563, 0.0932	0.0444, 0.0928	0.0443, 0.0785	0.0518, 0.0842	0.0800, 0.0971
Largest diff. peak and hole, e.Å <sup>-3</sup>	1.273, -0.618	1.624, -1.059	1.039, -0.687	1.302, -0.690	0.598, -0.513

Identification code	<b>1a</b>
Empirical formula	$C_{78}H_{96}Cr_2Fe_4N_4O_{24}Tb_2$
Formula weight	2118.82
Temperature, K	150(2)
Wavelength, Å	0.71073
Crystal system	Triclinic
Space group	P-1
$a$ , Å	10.0901(18)
$b$ , Å	12.780(3)
$c$ , Å	16.698(3)
$\alpha$ , °	105.437(6)
$\beta$ , °	96.248(6)
$\gamma$ , °	95.977(6)
Volume, Å <sup>3</sup>	2043.2(7)
$Z$	1
$D$ (calc), Mg/m <sup>3</sup>	1.722
$\mu$ , mm <sup>-1</sup>	2.728
$F(000)$	1066
Crystal size, mm	$0.08 \times 0.08 \times 0.02$
$\theta$ range, °	2.371, 25.349
Index ranges	-12 $\leq$ h $\leq$ 12 -15 $\leq$ k $\leq$ 15 -20 $\leq$ l $\leq$ 20
Reflections collected	26431
Independent reflections, $R_{int}$	7475, 0.1715
Completeness to $\theta = 25.242^\circ$	99.9 %
Absorption correction	Semi-empirical from equivalents
Max., min. transmission	0.0439, 0.0223
Refinement method	Full-matrix least-squares on $F^2$
Data / restraints / parameters	7475 / 0 / 478
Goodness-of-fit	0.946
$R_1$ , $wR_2$ [ $I > 2\sigma(I)$ ]	0.0691, 0.1290
$R_1$ , $wR_2$ (all data)	0.1693, 0.1655
Largest diff. peak and hole, e.Å <sup>-3</sup>	1.601, -1.928

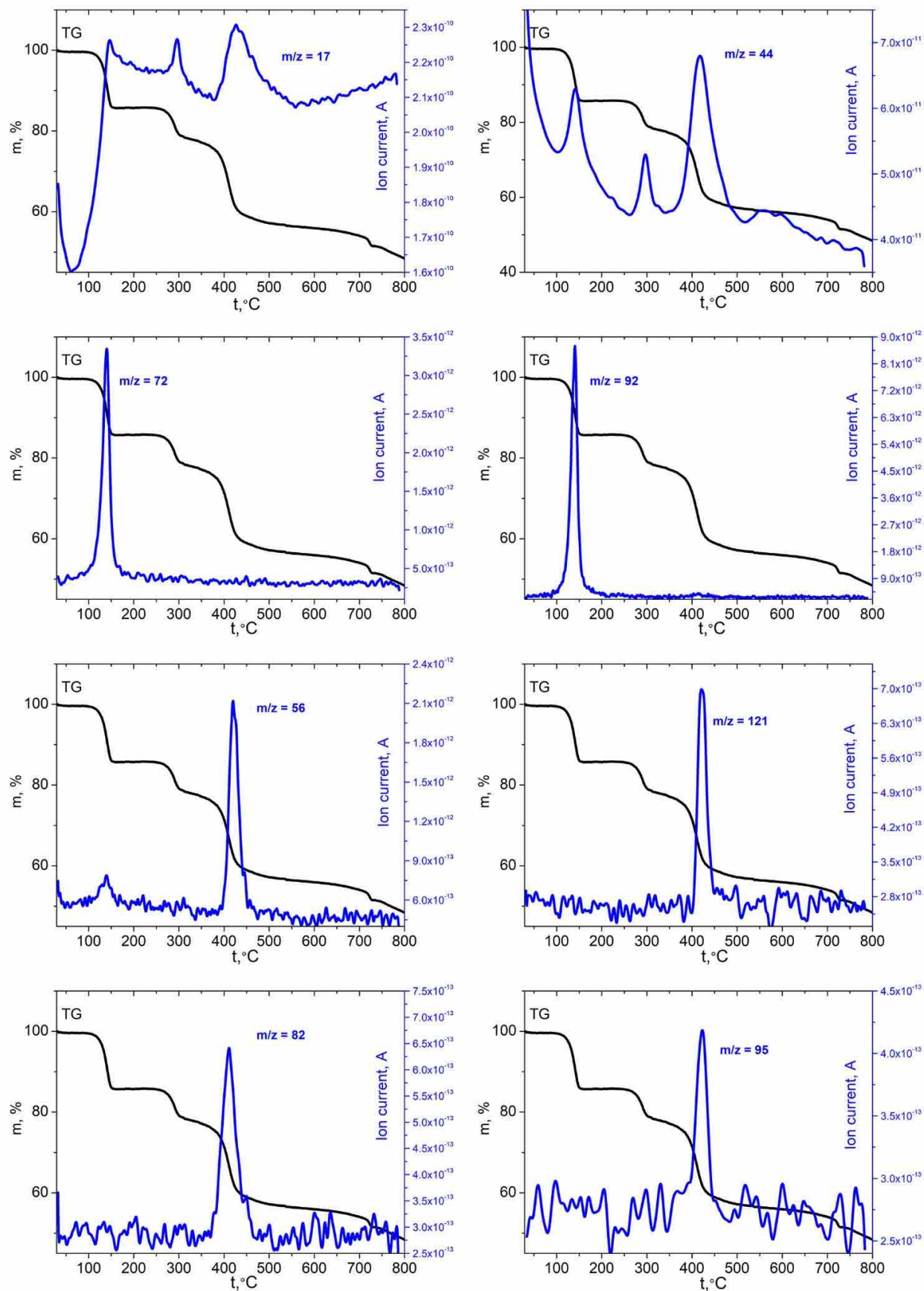


**Fig. S1.** Ionic currents in the mass spectrum of the gases evolved during thermolysis of Ho complex **3** under argon.

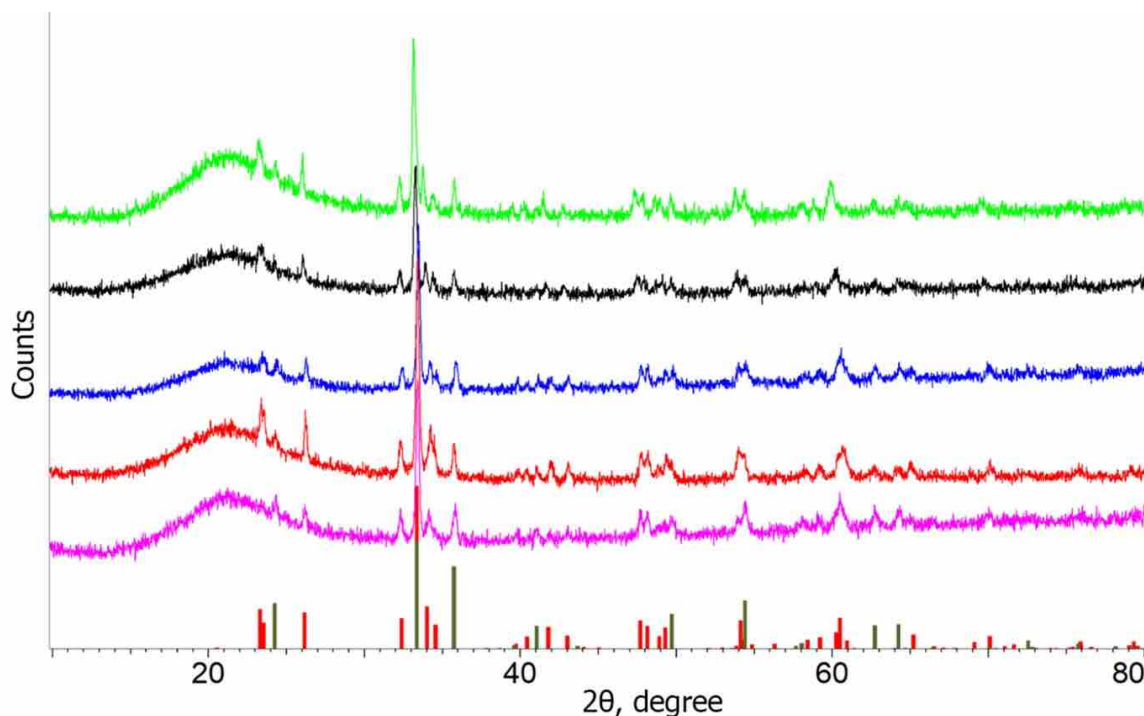


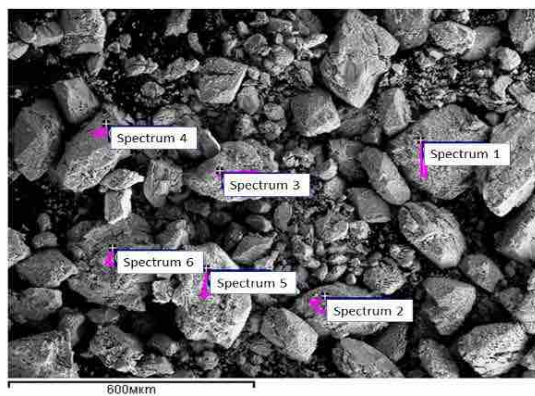
**Fig. S2.** Powder X-ray diffraction patterns of solid oxidative thermolysis products from complexes **1** (green line), **2** (black line), **3** (blue line), **4** (red line), and **5** (magenta line). Vertical sticks represent the X-ray diffraction patterns of  $\text{DyCrO}_3$  (red sticks), and  $\text{Cr}_{0.75}\text{Fe}_{1.25}\text{O}_3$  (brown sticks; taken from COD/PDF database, numbers COD 1008154 and PDF 01-077-9861, respectively).

**Table S2a** (see caption below).

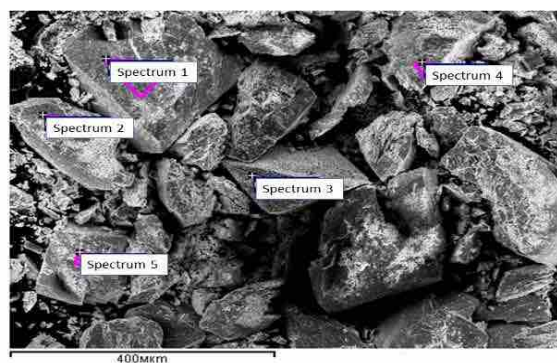
Spectrum	Cr	Fe	Tb
Spectrum 1	22.35	55.73	21.93
Spectrum 2	21.35	55.99	22.65
Spectrum 3	21.26	55.93	22.81
Spectrum 4	21.23	55.90	22.87
Spectrum 5	21.34	56.02	22.64
Spectrum 6	21.28	55.84	22.88
Mean	21.47	55.90	22.63

**Table S2b.**

Spectrum	Cr	Fe	Dy
Spectrum 1	25.02	51.18	23.80
Spectrum 2	26.17	47.93	25.90
Spectrum 3	25.16	50.59	24.25
Spectrum 4	25.02	50.84	24.14
Spectrum 5	23.06	53.44	23.50
Mean	24.75	50.98	24.27



**Fig. S3a** (see caption below).

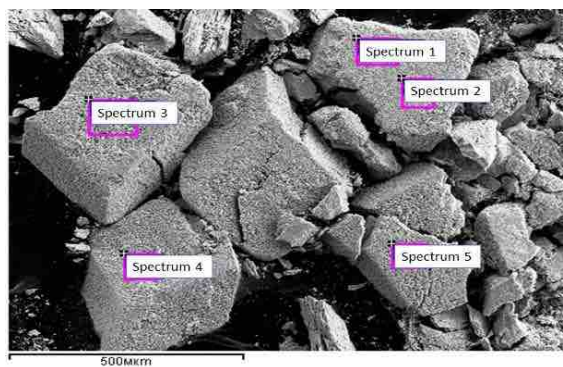


**Fig. S3b.**

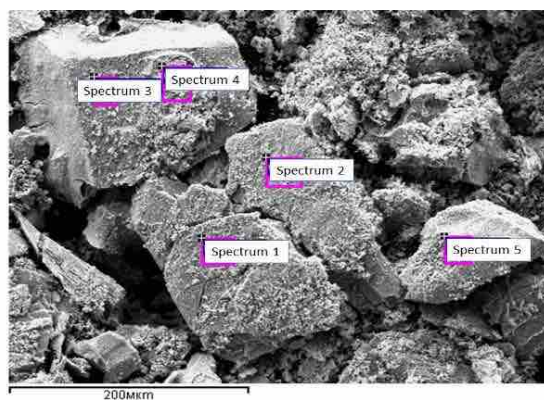


**Table S2c.**

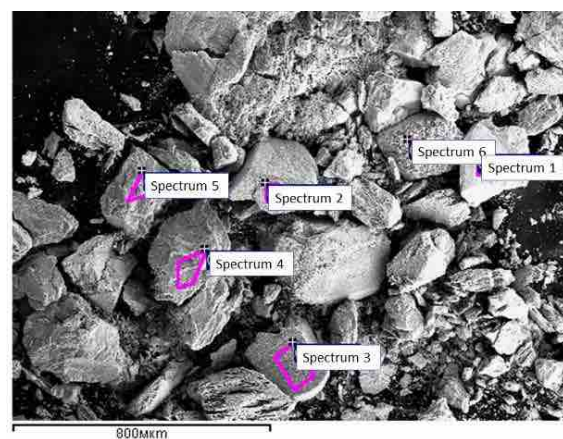
Spectrum	Cr	Fe	Ho
Spectrum 1	25.01	49.87	25.13
Spectrum 2	24.72	49.97	25.31
Spectrum 3	24.88	50.05	25.07
Spectrum 4	24.76	50.09	25.15
Spectrum 5	24.95	49.79	25.26
Mean	24.86	49.95	25.18

**Fig. 3c.****Table S2d.**

Spectrum	Cr	Fe	Er
Spectrum 1	24.58	51.05	24.37
Spectrum 2	24.53	50.50	24.97
Spectrum 3	24.29	50.74	24.97
Spectrum 4	25.44	48.02	26.54
Spectrum 5	24.64	50.81	24.55
Mean	24.70	50.21	25.09

**Fig. 3d.****Table S2e.**

Spectrum	Cr	Fe	Y
Spectrum 1	25.30	48.00	26.70
Spectrum 2	25.95	50.06	23.99
Spectrum 3	26.35	50.00	23.65
Spectrum 4	26.12	49.91	23.97
Spectrum 5	25.97	49.93	24.11
Spectrum 6	25.99	50.01	24.01
Mean	25.95	49.65	24.40

**Fig. 3e.**

**Tables 2a-e; Figs. S3a-e.** Energy dispersive X-ray microanalyses data (Tables, at.%) and corresponding SEM images for oxidative thermolysis products of complexes 1-5.

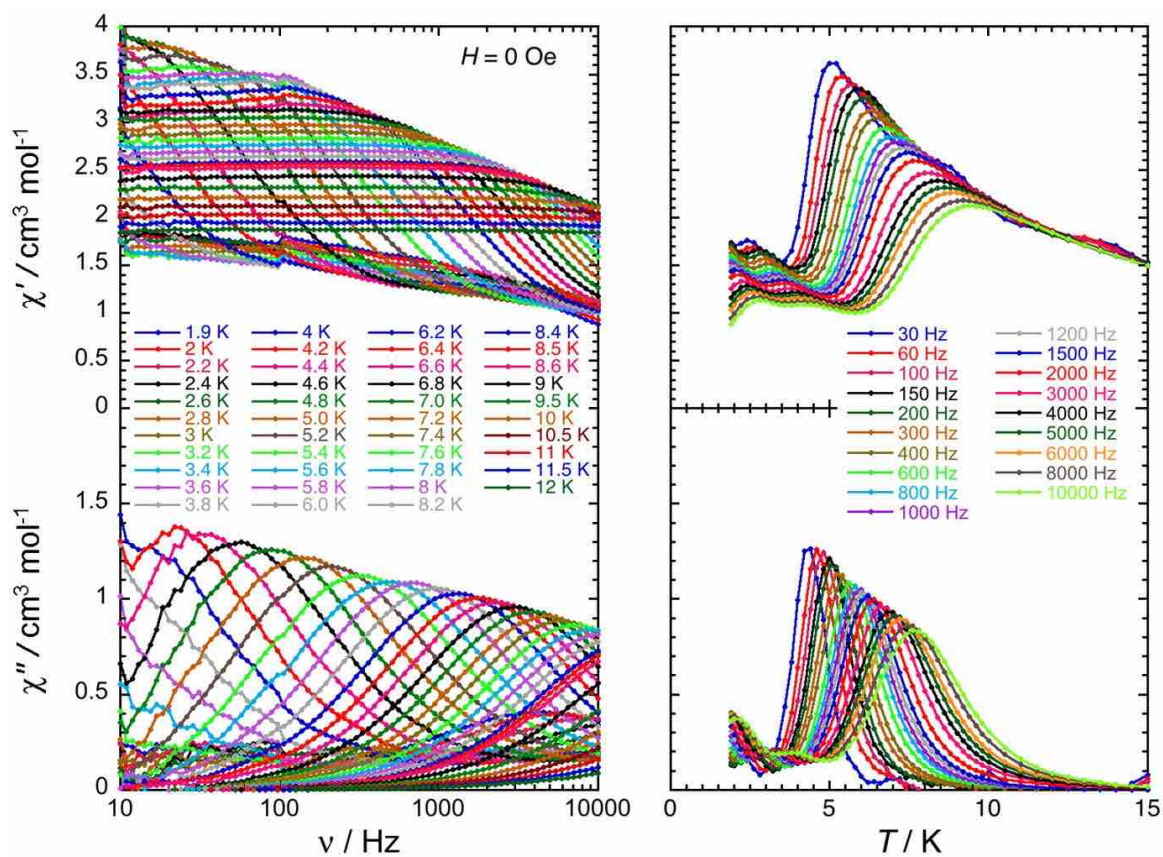


**Fig. S4.** ac frequency (left) and temperature (right) dependences of the real ( $\chi'$ , top) and imaginary ( $\chi''$ , bottom) parts of the ac susceptibility for **1** in zero-dc field and for ac frequencies between 10 and 10000 Hz and between 1.9 and 12 K.

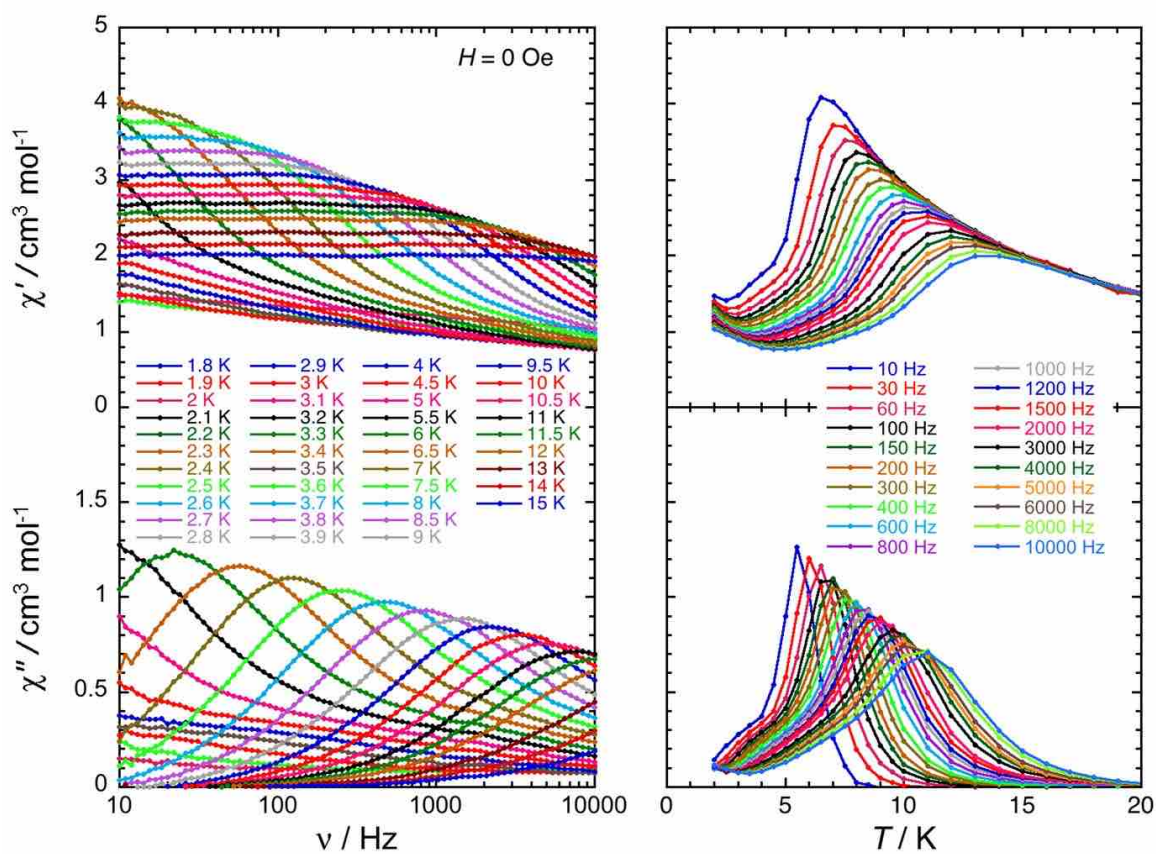


**Fig. S5.** ac frequency (left) and temperature (right) dependences of the real ( $\chi'$ , top) and imaginary ( $\chi''$ , bottom) parts of the ac susceptibility for **2** in zero-dc field and for ac frequencies between 10 and 10000 Hz and between 1.8 and 15 K.

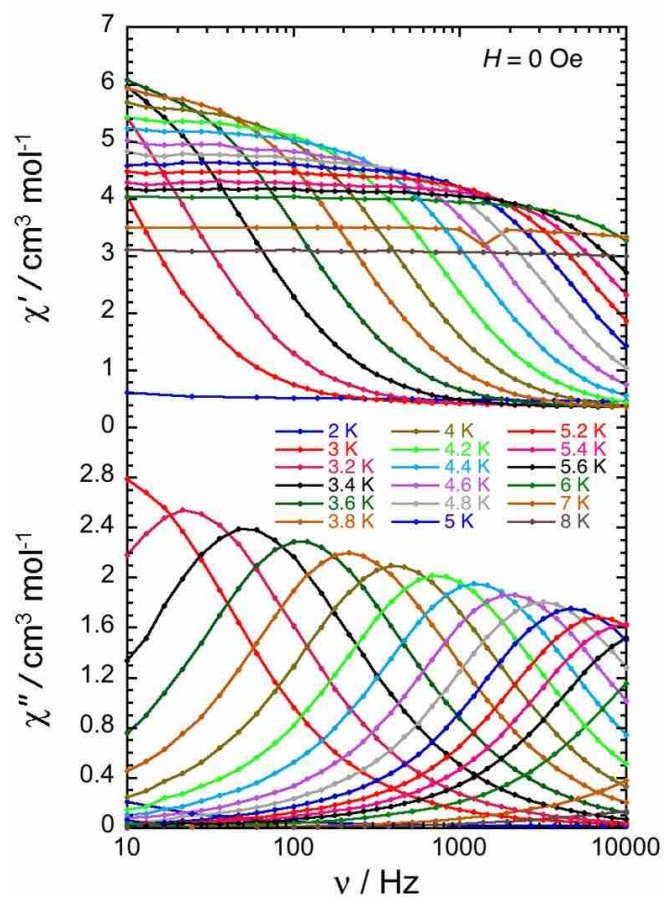


**Fig. S6.** ac frequency dependence of the real ( $\chi'$ , top) and imaginary ( $\chi''$ , bottom) parts of the ac susceptibility for **3** in zero-dc field and for ac frequencies between 10 and 10000 Hz and between 2 and 8 K.

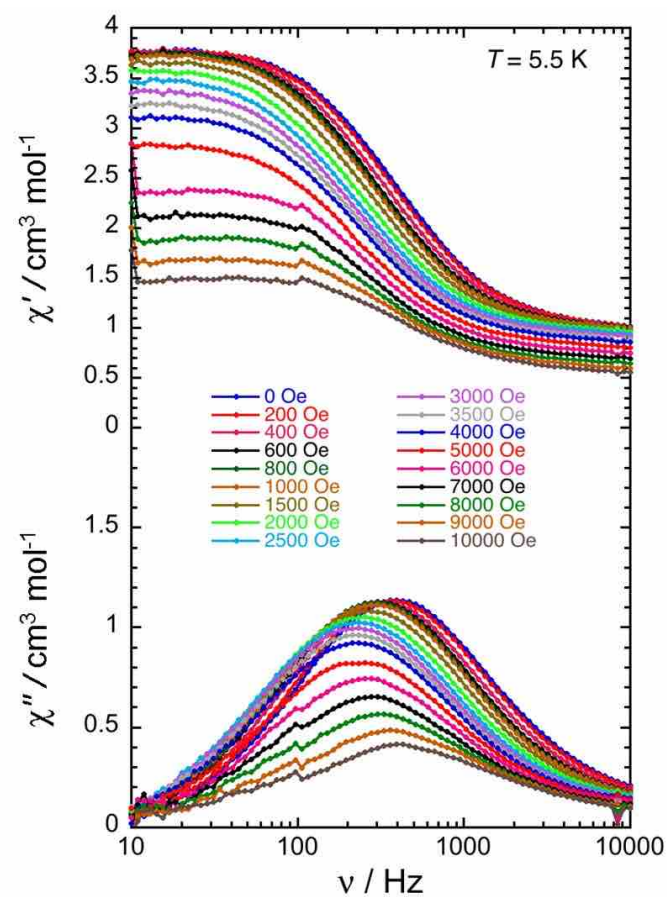


**Fig. S7.** ac frequency dependence of the real ( $\chi'$ , top) and imaginary ( $\chi''$ , bottom) parts of the ac susceptibility for **1** at 5.5 K under different dc fields between 0 and 1 T and for ac frequencies between 10 and 10000 Hz.

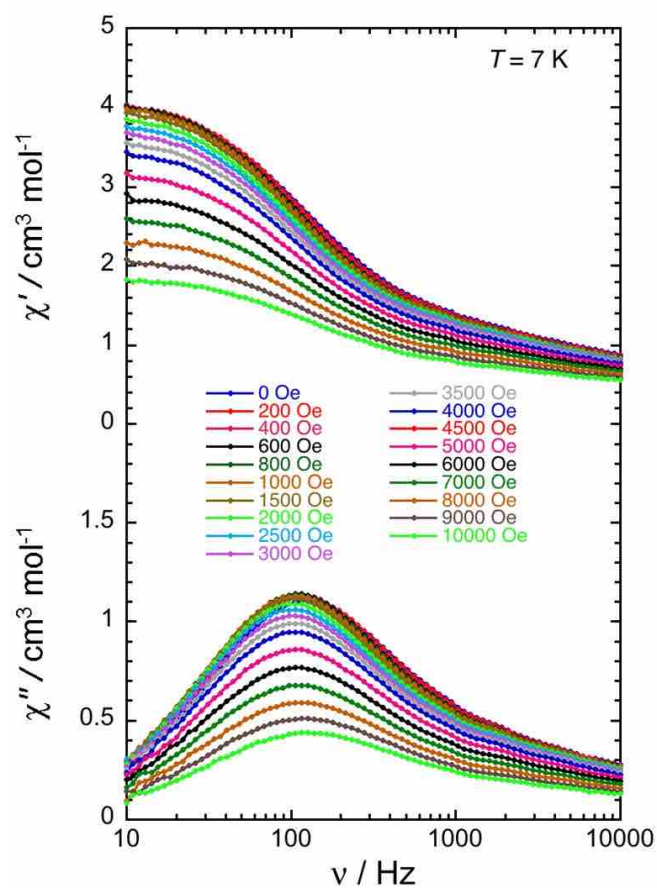


**Fig. S8.** ac frequency dependence of the real ( $\chi'$ , top) and imaginary ( $\chi''$ , bottom) parts of the ac susceptibility for **2** at 7 K under different dc fields between 0 and 1 T and for ac frequencies between 10 and 10000 Hz.

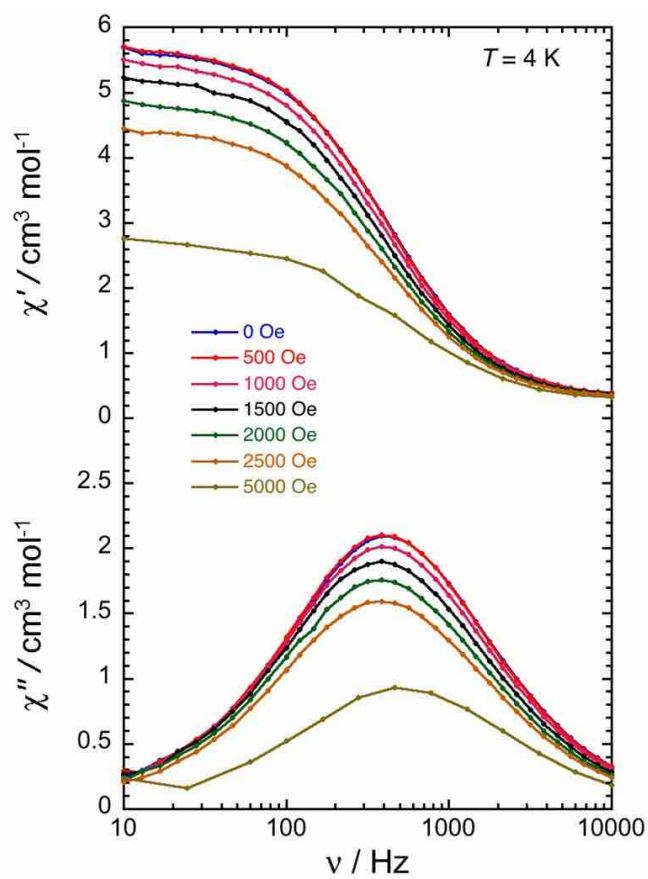


**Fig. S9.** ac frequency dependence of the real ( $\chi'$ , top) and imaginary ( $\chi''$ , bottom) parts of the ac susceptibility for **3** at 4 K under different dc fields between 0 and 0.5 T and for ac frequencies between 10 and 10000 Hz.

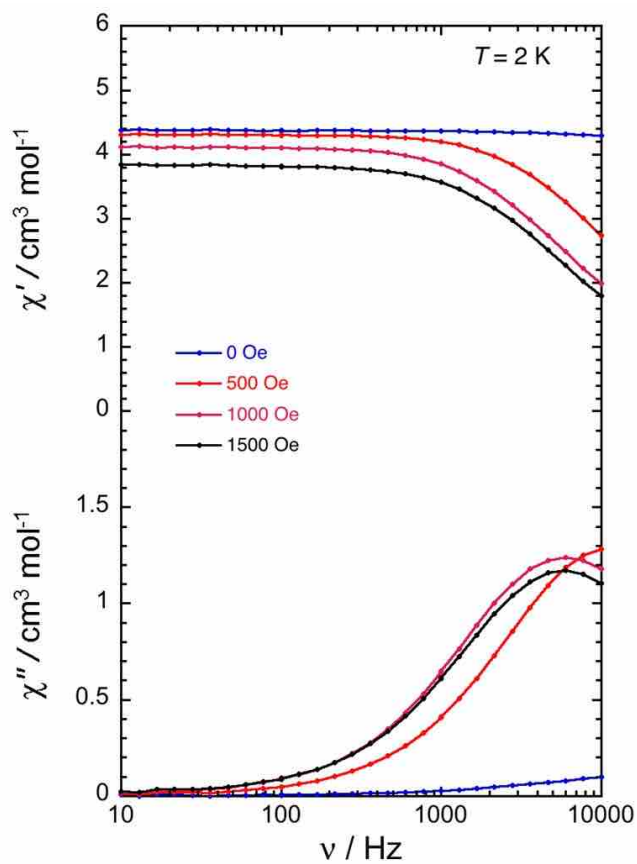


**Fig. S10.** ac frequency dependence of the real ( $\chi'$ , top) and imaginary ( $\chi''$ , bottom) parts of the ac susceptibility for **4** at 2 K under different dc fields between 0 and 0.15 T and for ac frequencies between 10 and 10000 Hz.